Modern and late Pleistocene particulate organic carbon transport by the Amazon River: Insights from long-chain alkyl diols

Christoph Häggi [a,b,*], Enno Schefuß [b], André O. Sawakuchi [c], Cristiano M. Chiessi [d], Stefan Mulitza [b], Dailson J. Bertassoli Jr. [c], Jens Hefter [e], Matthias Zabel [b], Paul A. Baker [f], Stefan Schouten [a,g]

[a] *NIOZ, Royal Netherlands Institute for Sea Research, Department of Marine Microbiology and Biogeochemistry (MMB), and Utrecht University, PO Box 59, 1790 AB Den Burg, the Netherlands*
[b] *MARUM – Center for Marine Environmental Sciences, University of Bremen, Leobener Str. 8, 28359 Bremen, Germany*
[c] *Institute of Geosciences, University of São Paulo, Rua do Lago 562, 05508-080 São Paulo, SP, Brazil*
[d] *School of Arts, Sciences and Humanities, University of São Paulo, Av. Arlindo Bettio 1000, 03828-000 São Paulo, SP, Brazil*
[e] *Alfred Wegener Institute – Helmholtz Centre for Polar and Marine Research, Am Handelshafen 12, 27570 Bremerhaven, Germany*
[f] *Division of Earth and Ocean Sciences, Duke University, Durham, NC 27708, USA*
[g] *Utrecht University, Faculty of Geosciences, Department of Earth Sciences, Budapestlaan 4, 3584 CD Utrecht, the Netherlands*

Abstract

The relative abundance of the C_{32} 1,15 long-chain alkyl diol (LCD) is an emerging proxy for the input of riverine aquatic particulate organic carbon (POC) into coastal oceans. This compound has the potential to complement other established proxies reflecting riverine terrestrial POC input and allows for a more nuanced assessment of riverine POC export to coastal seas. The current understanding of this proxy is, however, limited. In this study, we compare different indices for riverine sediment input to coastal marine waters (i.e. C_{32} 1,15-LCD, BIT index and Fe/Ca ratio) in a source-to-sink assessment in the Amazon River drainage system and the northeast South American continental margin, and we test their down-core applicability in a marine gravity core containing late Pleistocene fluvial Amazonian sediments. We show that the relative abundance of the C_{32} 1,15-LCD is highest in water bodies with low flow velocity and low turbidity such as the downstream portion of lowland tributaries and floodplain lakes. Relative C_{32} 1,15-LCD abundance is lowest in Andean white water tributaries where autotrophic productivity is hindered by high turbidity and high flow velocity. We also find that suspended particulate matter from all major tributaries during the extreme 2015 dry season has a similar LCD distribution to that of floodplain lakes. This indicates that the chemical composition of the tributaries is less relevant for the LCD distribution than their physical properties such as flow velocity and turbidity. Results from marine surface sediments offshore the Amazon River estuary show significant positive correlations between all three studied proxies. In contrast, we find that the relative C_{32} 1,15-LCD abundance in the down-core record is anti-correlated to the BIT index and Fe/Ca ratio. While BIT index and Fe/Ca ratio show high (low) values during Heinrich stadials (Dansgaard-Oeschger interstadials), the C_{32} 1,15-LCD proxy shows the opposite signal. BIT values are also higher during Marine Isotope Stage (MIS) 2 than during MIS 3, in contrast to trends in the C_{32} 1,15-LCD proxy. We posit that this pattern arises from a reduction in relative C_{32} 1,15-LCD abundance and total LCD productivity in the Amazon River during MIS 2 when less-humid conditions and lower sea level led to reduced area

---

* Corresponding author at: Department of Earth Sciences, University of Southern California, 3651 Trousdale Pkwy, Los Angeles, CA 90089, USA.
E-mail address: haggi@usc.edu (C. Häggi).

of floodplains. During Heinrich stadials, Andean sediment input increased and led to higher turbidity that resulted in lower C_{32} 1,15-LCD production. Our study shows that major changes in water discharge, sediment transport and river morphology can lead to discrepancies between the BIT index and the relative abundance of the C_{32} 1,15-LCD. Thus, we suggest that Amazonian aquatic and terrestrial POC pools had contrasting responses to changes related to both climate (e.g. increased Andean precipitation) and river morphology (e.g. steeper along-channel slope due to falling and low stand sea level).

1. INTRODUCTION

The transport of particulate organic carbon (POC) by river systems provides an important link between terrestrial (e.g. soils) and marine (e.g. sediments) carbon reservoirs (Battin et al., 2008). The Amazon River and its tributaries are the largest fluvial system in the world and their annual transport of POC amounts to about 14×10^{12} g C y^{-1} (Richey et al., 1990; Galy et al., 2015), about 7% of the global riverine POC export (Galy et al., 2015). Most of the POC transported by rivers is soil- and rock-derived. In the Amazon River system, POC is predominantly sourced from soils in the lowland Amazon Basin. Rock-derived POC from the Andes is thought to contribute no more than 10% of the total POC (Hedges et al., 2000; Bouchez et al., 2014; Häggi et al., 2016). In addition, aquatic primary productivity in rivers and wetlands provides another source of POC in tropical rivers (Hedges et al., 1986). In the Amazon River system, extensive floodplains are the dominant source for aquatic POC and estimates suggest that aquatic POC represents up to 17% of the total POC exported to the Atlantic Ocean (Moreira-Turcq et al., 2013). However, past changes in aquatic primary productivity in large tropical rivers such as the Amazon River and its major tributaries are not well constrained. This is mainly due to a lack of suitable proxies for riverine aquatic productivity.

Recently, the analysis of the fractional abundance of long-chain alkyl diols (LCD) provided a novel approach to study variable contributions of aquatically produced riverine POC in coastal oceans (Versteegh et al., 2000; de Bar et al., 2016; Lattaud et al., 2017a,b). LCDs are produced by aquatic organisms such as diatoms and marine microalgae and their composition has been used to reconstruct past sea surface temperature conditions and upwelling intensity (de Leeuw et al., 1981; Sinninghe Damsté et al., 2003; Rampen et al., 2008, 2012). In marine sediments, the C_{28} 1,13 and 1,14, C_{30} 1,13, 1,14 and 1,15 and C_{32} 1,15-LCDs are usually detected. The C_{30} 1,15-LCD is typically the dominant component in tropical marine regions and is less abundant in colder environments, where the C_{28} and C_{30} 1,13-LCD are dominant (Rampen et al., 2012). This relationship has been used for the creation of the long chain diol index (LDI) temperature proxy (Rampen et al., 2012). C_{28} and C_{30} 1,14-LCD produced by *Proboscia* diatoms are abundant in upwelling regions. Consequently, the fractional abundance of C_{28} and C_{30} 1,14 have been used as proxy for upwelling intensity (Rampen et al., 2008).

In coastal areas, the C_{32} 1,15-LCD has been found to be especially abundant, while it is typically scarce in exclusively marine environments (Versteegh et al., 1997, 2000; de Bar et al., 2016). Further studies have shown that the C_{32} 1,15-LCD is predominantly produced in freshwater systems (Zhang et al., 2011; Lattaud et al., 2017b). Hence, the fractional abundance of the C_{32} 1,15 has been proposed as a proxy to reconstruct the input of riverine organic carbon into coastal seas (Lattaud et al., 2017b). In contrast to other compounds used as indicators of terrestrial or riverine POC input into coastal seas, such as branched glycerol dialkyl glycerol tetraethers (brGDGTs), lignin or plant waxes, the C_{32} 1,15-LCD is apparently not produced by terrestrial plants or in soils (Shimokawara et al., 2010; de Bar et al., 2016). Even though the dominant synthesizing organisms are as yet unknown, the C_{32} 1,15-LCD is likely produced by freshwater eustigmatophyte algae (Volkman et al., 1999; Rampen et al., 2014; Villanueva et al., 2014). In the Amazon River system, a previous study has indeed found enhanced relative abundances of the C_{32} 1,15-LCD in suspended sediments of the Amazon River compared to tropical marine sediments (Lattaud et al., 2017b). The C_{32} 1,15-LCD proxy has shown good agreement with proxies for terrestrial organic carbon input into coastal seas, such as the ratio of brGDGTs to isoprenoid GDGTs (i.e. Branched and Isoprenoid Tetraether (BIT) index) (de Bar et al., 2016; Lattaud et al., 2017a,b), which measures the input of soil and river-derived brGDGTs relative to the marine-derived isoprenoid GDGTs (Hopmans et al., 2004; Zell et al., 2013). Down-core reconstructions also showed good agreement between BIT index and the C_{32} 1,15-LCD proxy (Lattaud et al., 2017a). While C_{32} 1,15-LCDs are present in most studied riverine sediments, their relative contribution is highly variable (Lattaud et al., 2017b, 2018). The causes for this variability are however not well understood. In the Amazon River system, there is thus a lack of understanding concerning: (i) the environmental factors that influence the riverine LCD distribution; (ii) the present day coastal LCD composition of riverine derived material; and (iii) how the distribution of LCDs exported by the Amazon river changed in the past and the mechanisms controlling terrestrial and aquatic riverine POC export.

In order to better understand the factors controlling C_{32} 1,15-LCD productivity in riverine environments, we studied

suspended sediment samples from the Amazon River and its major tributaries. The Amazon tributaries drain a wide range of landscapes, giving origin to rivers with different characteristics (Sioli, 1984). To study the relationship between the relative abundance of the C_{32} 1,15-LCD and other proxies that reflect riverine organic and inorganic input to coastal seas, we collected marine sediment samples from sites close to the Amazon River estuary, with currently high sediment accumulation rates, and from sites currently not influenced by sediments derived from the Amazon River. Finally, we tested the fractional abundance of the C_{32} 1,15-LCD as a proxy to track past changes in Amazonian freshwater productivity during the late Pleistocene using a well-studied marine gravity core (i.e. GeoB16224-1) from the continental margin offshore of French Guiana, an area dominated by Amazon-derived sediment (Zhang et al., 2015). Previous studies on this sediment core showed high terrestrial sediment input during Heinrich stadials (HS) and Dansgaard-Oeschger stadials based on high-resolution X-ray fluorescence (XRF) data (Zhang et al., 2017). In this core, the BIT index during HS 1 is well correlated with the Fe/Ca elemental ratio, indicating increased input of inorganic sediment and terrestrial POC (Crivellari et al., 2018). Thus, core GeoB16224-1 offers an excellent opportunity to compare the C_{32} 1,15-LCD proxy to other proxies used as indicators for terrestrial input to assess how aquatic riverine POC behaves in relation to the much better studied terrestrial POC.

2. METHODS

2.1. Study area

The Amazon region hosts the largest river system in the world, which predominantly drains areas covered by tropical rainforest. The Amazon River rises in the Andes and flows through an extensive lowland basin across northern South America before discharging into the western equatorial Atlantic (Fig. 1). While most of the water from the Amazon River is derived from lowland areas (McClain and Naiman, 2008), approximately 90% of the suspended sediment transported by the Amazon River originates in the Andes, dominantly from two large tributaries, the Madeira and Solimões rivers (Meade et al., 1985). Due to their light brown colour caused by the high suspended sediment load, both rivers are classified as white water rivers (Sioli, 1984). The characteristics of lowland tributaries are not homogenous. On the one hand, lowland tributaries from the western Andean foreland like the Jutaí and Juruá rivers can also be classified as white water tributaries. On the other hand, there are "clear water" tributaries such as the Tapajós and Xingu rivers that drain cratonic shield areas in the eastern lowland and transport only small amounts of suspended sediments (McClain and Naiman, 2008). Lowland "black water" tributaries such as the Negro River drain extensive wetlands and are named for their dark coloured waters that stem from their high amount of dissolved organic carbon (Konhauser et al., 1994). In this study, we also regard the Purus River as a black water river, since it has black water characteristics during the studied dry season, while white water characteristics dominate during the wet season (Salimon et al., 2013). Therefore, it is important to note that some lowland white water tributaries can become black or clear water rivers during lowwater stages, when water run-off and soil erosion are reduced. Finally, we present data from the Japurá and Içá rivers. Both tributaries have their westernmost headwaters in the Colombian Andes. Their sediment load and basinwide erosion are much lower than for the Solimões and Madeira rivers and their characteristics resemble the
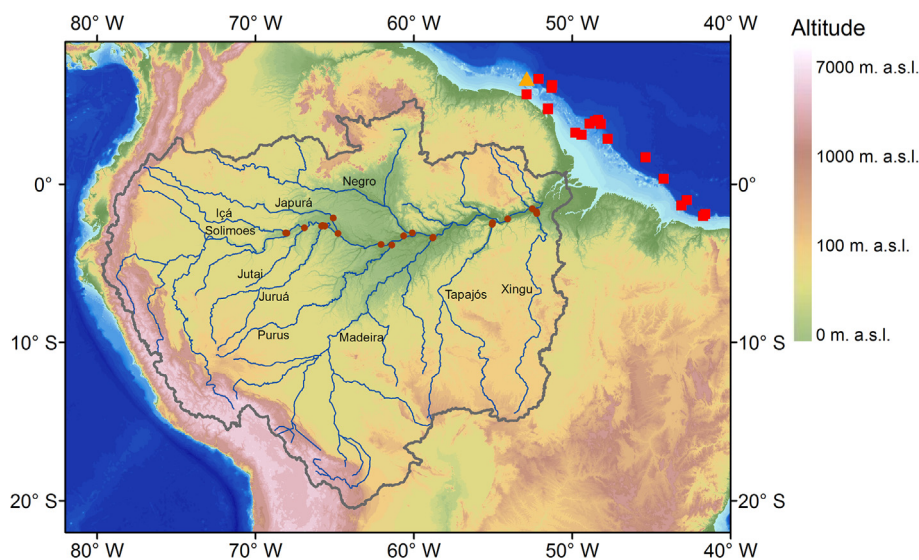

Fig. 1. Topographical map of the Amazon Basin and the adjacent Atlantic Ocean. Marine surface sediment samples used for this study are marked with red squares. Core GeoB16224-1 used in the study is marked with an orange triangle. The sites of suspended sediment samples from the Amazon River and its tributaries are marked with brown circles. The extent of the Amazon Basin is marked with a dark gray line. Note the logarithmic color scale for the altitude. (For interpretation of the references to colour in this figure legend, the reader is referred to the web version of this article.)

lowland white water Juruá or Jutaí rivers (Latrubesse et al., 2017). Hence, we classify both tributaries together with the Juruá and Jutaí rivers as lowland white water rivers. Nutrient availability is higher in the white water rivers than in clear and black water tributaries (McClain and Naiman, 2008). Primary productivity, however, is highest in lowland tributaries and floodplain lakes (i.e. *Várzea* lakes), since the high sediment load in white water rivers leads to light limitation that impedes autotrophic productivity (Wissmar et al., 1981). Indeed, water transparency in white water tributaries is significantly lower (10–50 cm secchi disk depth) than in black (130–290 cm) and clear water tributaries (110–430 cm) (Sioli, 1984). A similar pattern is also seen for euphotic depth, which varies between 50 cm (rising water season) and 120 cm (receding water season) in white water rivers, while it is greater in black water (190 cm in rising water season and 540 cm in receding water season) and clear water tributaries (260 cm in rising water season and 590 cm in receding water season) (Costa et al., 2013). The different tributaries also have variable water chemistry as indicated by their different pH values. White water tributaries typically have pH between 6 and 7, clear water tributaries have pH between 5 and 8, and black water tributaries have the lowest pH values, between 4 and 5 (Sioli, 1984).

After discharge into the western equatorial Atlantic, water and sediment from the Amazon River are entrained in the North Brazil Current and advected north-westward along the northernmost Brazilian and Guianan margins (Muller-Karger et al., 1988). Most of the modern Amazon-derived marine sedimentation takes place either on the Amazon subaqueous delta or in other sectors of the continental shelf located northwest of the delta (Geyer et al., 1996). Regions situated south-east of the Amazon River estuary do not receive modern Amazonian sediments (Zhang et al., 2015; Häggi et al., 2016). Likewise, there is little modern sedimentation of Amazonian material taking place on the continental slope. This scenario contrasts with sedimentation loci during glacial periods, when large quantities of terrestrial sediment bypassed the shelf and were deposited on the continental slope offshore the Amazon and French Guiana (Damuth and Flood, 1983). Thus, the sediments deposited on the continental slope constitute a highly resolved archive for determining late Pleistocene changes in Amazonian climate and hydrology (Loncke et al., 2009; Mulitza et al., 2013; Nace et al., 2014; Häggi et al., 2017; Zhang et al., 2017; Crivellari et al., 2018).

2.2. Sampling

Suspended sediment samples (Fig. 1; see Appendix A for sample coordinates) were collected using a submersible water pump coupled to a hose. Suspended sediment samples were taken in the channel thalweg. Except for two samples obtained in 1 m water depth, samples were taken in 60% of the total water column depth. This depth was chosen as representative of average conditions in terms of suspended sediment content and flow velocity (Gordon et al., 2004). Due to variable organic matter yield, smaller samples of 30–50 litres were taken in the white water and black

water tributaries, while larger samples of 50–100 litres were taken in the clear water tributaries that transport less POC. After pumping water from the river channel, most of the water was removed using a Merck Millipore Ultrafiltration system equipped with Pellicon 2 Ultrafiltration cassettes coupled to a Masterflex easy load II pump head until the sample volume was condensed below 1 litre. The samples were then transferred to 1 litre teflon bottles and frozen on-board.

Marine surface sediment samples (Fig. 1; see Appendix B for sample coordinates, and depth) used in this study are described in detail in Häggi et al. (2016) and Mulitza et al. (2013). In short, the samples were collected using a multi corer during *RV Maria S. Merian* cruise MSM20/3 in February and March 2012 and during the *RV Knorr* cruise KNR/97-4 in February and March 2010. Marine surface sediments were taken from the Amazon outflow, the shelf area below the Amazon plume, the Amazon subaqueous delta, as well as areas offshore north-eastern Brazil that are currently not under the influence of Amazonian sediments (Zhang et al., 2015).

Gravity core GeoB16224-1 was collected during *RV Maria S. Merian* cruise MSM20/3 in March 2012. Detailed description of the core can be found in Mulitza et al. (2013), while the age model used for the core is described in Häggi et al. (2017) based on the data presented in Zhang et al. (2015). Briefly, the core was taken from the continental slope off French Guiana (6°39.38′N, 52°04.99′W; 760 cm core length; 2510 m water depth) and covers the late Pleistocene (12.8–49 ka BP) in a high temporal resolution (Zhang et al., 2015; Häggi et al., 2017).

2.3. Methodological approach

As a measure for the relative abundance of different LCDs, we followed Lattaud et al. (2017a,b):

$$\%\text{Diol}_x = \frac{A Diol_x}{AC_{32}\,1,15 + AC_{30}\,1,15 + AC_{30}\,1,14 + AC_{30}\,1,13 + AC_{28}\,1,14 + AC_{28}\,1,13} \times 100 \tag{1}$$

where A represents the integrated peak area of the respective LCD.

We applied the LDI as a proxy for temperature (Rampen et al., 2012):

$$LDI = \frac{AC_{30}1,15}{AC_{28}\,1,13 + AC_{30}\,1,13 + AC_{30}\,1,15} \tag{2}$$

and converted this to mean annual sea surface temperature (SST) using the following equation (Rampen et al., 2012):

$$\text{Mean annual SST} = \frac{LDI - 0.095}{0.033} \tag{3}$$

The BIT index was used as a measure for input of soil and riverine organic matter into the coastal ocean. The BIT index describes changes in the relative amount of branched GDGT (produced by soil and river bacteria) and the isoprenoid GDGT Crenarchaeol (produced predominantly by marine archaea) (Hopmans et al., 2004):

$$BIT = \frac{brGDGTI + brGDGTII + brGDGTIII}{brGDGTI + brGDGTII + brGDGTIII + GDGTIV}$$

$$(4)$$

To track the input of inorganic terrestrial sediment to the coastal ocean, the Fe/Ca ratio is commonly used (Govin et al., 2012). In the Amazon River system, sediments have Ca contents <10% (Zhang et al., 2017). Hence, in marine sediments off the Amazon plume, Ca is mostly of marine carbonate origin, while Fe is mostly of terrestrial origin. For better comparability of the Fe/Ca data with the BIT index and the % C_{32} 1,15 data, we used a notation similar to the BIT index and defined the CAFE index as follows:

$$CAFE\ index = \frac{\%Fe}{\%Ca + \%Fe} \qquad (5)$$

Finally, we compared the proxy data to bulk $\delta^{13}C$ data of the same samples by Sun et al. (2017), which can also be used to track the relative amount of terrestrial organic matter to Amazonian offshore areas.

2.4. Laboratory procedures

The frozen suspended sediment samples were freeze dried in an Alpha Christ freeze drier in order to remove the remaining water. Aliquots of suspended sediments containing 0.07–4.5 g of sediment were extracted with an ASE 300 Accelerated Solvent Extractor for three cycles (100 °C, 1000 psi) using Dichloromethane (DCM):Methanol (MeOH) 9:1 (v:v) as solvents. Known amounts of C_{46} glycerol trialkyl glycerol tetraether and C_{22} 7,16-LCD were added as internal process standards for GDGT and LCD quantification after extraction. Total lipid extracts (TLEs) were dried under nitrogen. Subsequently, residual water was removed over columns of Na_2SO_4 using DCM as solvent. The TLEs were then methylated in 0.5 ml BF_3-methanol at 60 °C for 10 min. TLEs were recovered using liquid-liquid extraction using DCM and bi-distilled water. TLEs were again cleaned over Na_2SO_4 to remove remaining traces of water. Compounds were then separated over columns of 4 cm of aluminium oxide. Elution of TLEs with hexane, DCM and DCM:MeOH 9:1 yielded hydrocarbon, ketone/FAME and polar fractions. Subsequently, the polar fraction was split into two sub-fractions for LCD and GDGT analysis. The fraction for GDGT analysis was filtered through PTFE syringe filters (4 mm, 0.45 μm) in preparation for measurement. The preparation procedure for surface sediment samples and sediment samples from GeoB16224-1 is described in Häggi et al. (2016, 2017).

Prior to LCD analysis, silylation of the polar fraction was performed by dissolving the sample in 10 μl N,O-bis(tri methylsilyl)trifluoroacetamide (BSTFA) and 10 μl pyridine and heating it for 30 min at 60 °C. After cooling, 30 μl of ethyl acetate was added. LCD analysis was performed on an Agilent Technologies 7890B Gas Chromatograph (GC) coupled to an Agilent Technologies 5977A Mass Selective Detector (MSD) and equipped with a CP-Sil 5 CB capillary silica column (25 m × 0.32 mm; 0.12 μm film thickness). LCDs were detected using selective ion monitoring (SIM).

The SIM detector was set for m/z 187.0, 299.4, 313.4, 327.4 and 341.4. Every 5 samples a full scan analysis of m/z 50 to 850 was run to confirm the presence of LCDs in SIM measurements. Quantification of LCDs from the suspension samples was achieved by comparison of peak areas to the internal C_{22} 7,16-LCD standard.

Branched and isoprenoid GDGTs were analyzed by liquid chromatography (LC) coupled via an atmospheric pressure chemical ionization (APCI) interface to a single quadrupole mass spectrometer (MS). Core and marine surface sediment samples were measured with a method slightly modified from Hopmans et al. (2000), while river suspended sediment samples were analysed according to the method described in Hopmans et al. (2016). Analyses were performed on an Agilent 1200 series HPLC system and an Agilent 6120 MSD. Detailed description of the measurements can be found in Crivellari et al. (2018).

Fe and Ca concentrations were measured using energy dispersive polarization X-ray fluorescence (EDP-XRF) spectroscopy. Analysis was conducted on 3–4 g of dry sediment powder with a PANalytical Epsilon 3XL instrument. Analytical quality was assessed by repeated analyses of the certified standard reference material MAG-1. The measured values were within 1% of the accepted value for Ca and Fe. The standard deviation of replicates was less than 0.6%. The methodology for additional XRF scanner data for core depth from 600- 760 cm in core GeoB16224-1 is described in Zhang et al. (2017).

2.5. Statistical analyses

Statistical analyses presented in the manuscript were conducted with the statistical software PAST version 3.16 (Hammer et al., 2001). These include principal component analysis (PCA) of the LCD distribution and r^2 and p-values for linear regressions. PCA was conducted using the spectral decomposition approach.

3. RESULTS

3.1. Suspended sediments

Results of LCD measurements on suspended sediment from the Amazon River showed relative abundances of the C_{32} 1,15-LCD (% C_{32} 1,15) over 40%, while the relative abundance of the second most abundant compound, the C_{30} 1,15-LCD varied between 10 and 30% (Fig. 2a, b; 3a, b; see Appendix A for raw data, sample coordinates and sample depth). Fractional abundances of the remaining LCDs (i.e. C_{28} 1,13 and 1,14, and C_{30}, 1,13 and 1,14) were < 10%. The highest % C_{32} 1,15 values were found in suspended sediment from the lowland white water tributaries (i.e. 58–85%, Fig. 2a). Suspended sediment from the clear water tributaries showed fractional amounts of 59–64%, samples from black water tributaries showed fractional abundances of 46–48% and samples from the white water tributaries showed fractional abundances of 44–57% (Fig. 2a). Fractional abundances of the C_{30} 1,15-LCD displayed the opposite pattern with lower abundances in lowland white water tributaries and higher abundances
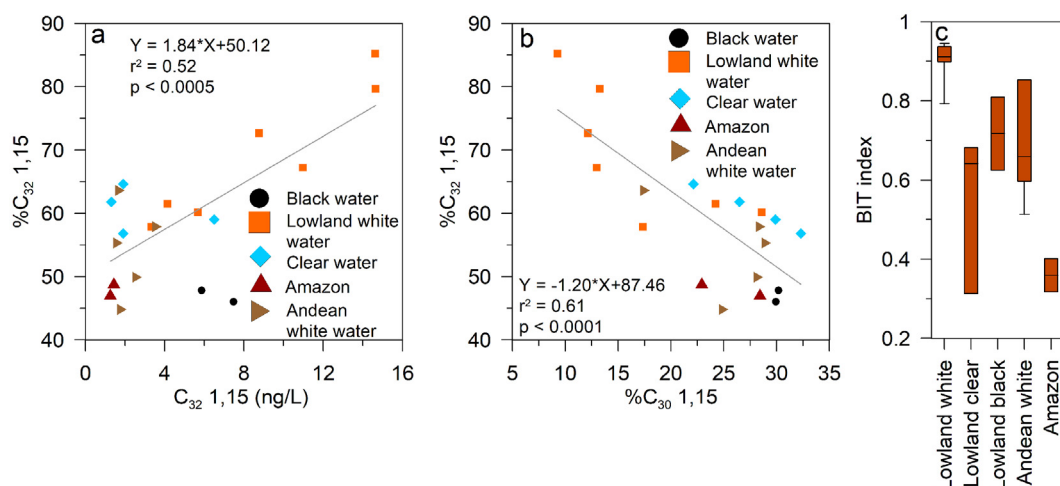
Fig. 2. Long-chain alkyl diol (LCD) distribution and concentrations in suspended sediment samples from the Amazon River system. (a) Relationship between $\%C_{32}$ 1,15 and absolute C_{32} 1,15 concentrations. (b) Relationship between $\%C_{32}$ 1,15 and $\%C_{30}$ 1,15. (c) Box plots of BIT index in the different types of tributaries of the Amazon River. Lowland white water tributaries include Juruá, Jutaí, Içá and Japurá rivers (samples $n = 7$). Lowland black water tributaries include the Negro and Purus rivers (samples $n = 2$), whereas the Purus River changes its characteristics seasonally (Salimon et al., 2013). Andean white water tributaries are the Madeira and Solimões rivers (samples $n = 5$), while the lowland clear water tributaries are the Tapajós and Xingu rivers (samples $n = 4$). Samples from the Amazon River main stem (n = 2) were taken close to the estuary.

in the Andean white water rivers and the cratonic lowland rivers (Fig. 2b). Absolute C_{32} 1,15 concentrations varied between 4 and 15 ng/L in the lowland white water tributaries, while concentrations were lower in the cratonic clear water tributaries (1–6 ng/L), black water tributaries (6–8 ng/L), and Andean white water tributaries (1–4 ng/L) (Fig. 2a). BIT values varied between 0.3 and 0.95 (Fig. 2c).

3.2. Marine surface sediments

In marine surface sediment $\%C_{32}$ 1,15 varied between 1 and 20%, with maximum values found on the Amazon subaqueous delta and the Guyana shelf (Fig. 4a; see Appendix B for raw data and sample coordinates). Sediments from outside this area show distinctly lower values <5%. BIT index values varied between 0.05 and 0.7, with the highest values on the Amazon subaqueous delta and the Guyana shelf and values <0.2 in areas with no modern accumulation of sediments from the Amazon River (Fig. 4b). BIT index values thus reveal a similar pattern as the $\%C_{32}$ 1,15 values. The CAFE index varied between 0.01 and 0.9. The highest values were found on the Amazon subaqueous delta and the Guianan shelf, while lower values are found offshore north-eastern Brazil (Fig. 4c). Samples from the continental slope off French Guiana show intermediate values. $\%C_{32}$ 1,15 values and the BIT index are positively correlated ($r^2 = 0.66$, $p < 10^{-4}$; Fig. 5a). $\%C_{32}$ 1,15 values and BIT indices are also positively correlated with the CAFE indices ($r^2 = 0.66$, $p < 10^{-4}$ for C_{32} 1,15 vs. CAFE index; $r^2 = 0.51$, $p < 0.001$ for BIT index vs. CAFE index; Fig. 5g and h). We also find significant correlations between other long chain alkyl LCDs and the BIT index (Fig. 5b–e). The fractional abundances of the C_{30} 1,14 and the C_{30} 1,13-LCDs ($\%C_{30}$ 1,14 and $\%C_{30}$ 1,13) show a positive correlation with the BIT index ($r^2 = 0.45$;

$p < 0.002$ for the C_{30} 1,14-LCD; $r^2 = 0.44$; $p < 0.003$ for the C_{30} 1,13-LCD; Fig. 5c and d). Finally, we find that the fractional abundance of the C_{30} 1,15-LCD is anticorrelated with the BIT index ($r^2 = 0.40$; $p < 0.005$; Fig. 5b). The fractional abundance of the C_{28} 1,14-LCD ($\%C_{28}$ 1,14) was uncorrelated with the BIT index (Fig. 5e) and the fractional abundance of the C_{28} 1,13-LCD ($\%C_{28}$ 1,13) was <4% in all samples. LDI values varied from 0.8 to 1 and were lower on the continental shelf than in areas outside the influence of the Amazon River plume and anti-correlated with BIT indices (Fig. 5f). Reconstructed temperatures vary from 24 °C on the shelf to 29 °C in areas outside the influence of the Amazon plume (Fig. 5f). The comparison between the BIT index and existing bulk organic carbon $\delta^{13}C$ data from these samples also yielded a strong negative correlation ($r^2 = 0.90$; $p < 10^{-8}$ Fig. 5i). PCA analysis of the diol distribution of marine surface sediments shows opposite loadings in principal component (PC)1 (accounting for 89% of the variability) for the C_{30} 1,15-LCD compared to the rest of the studied LCDs (Fig. 9a).

3.3. Marine gravity core GeoB16224-1

In addition to the BIT index values reported in Crivellari et al. (2018) for sediment core GeoB16224-1, we provide new BIT index data for the periods between 12.8 and 14 ka BP, as well as between 22 and 49 ka BP. Similar to the trend during HS1, the new BIT index data shows elevated values up to 0.8 during HS 3, 4 and 5 (Fig. 6d; see Appendix C for raw data). Furthermore, distinct minima with values around 0.35 correspond to Dansgaard-Oeschger interstadials (DOI) (Fig. 6a and d). The variation during HS and DOI corresponds to what was observed in the CAFE index (Zhang et al., 2017, Fig. 6c). In addition
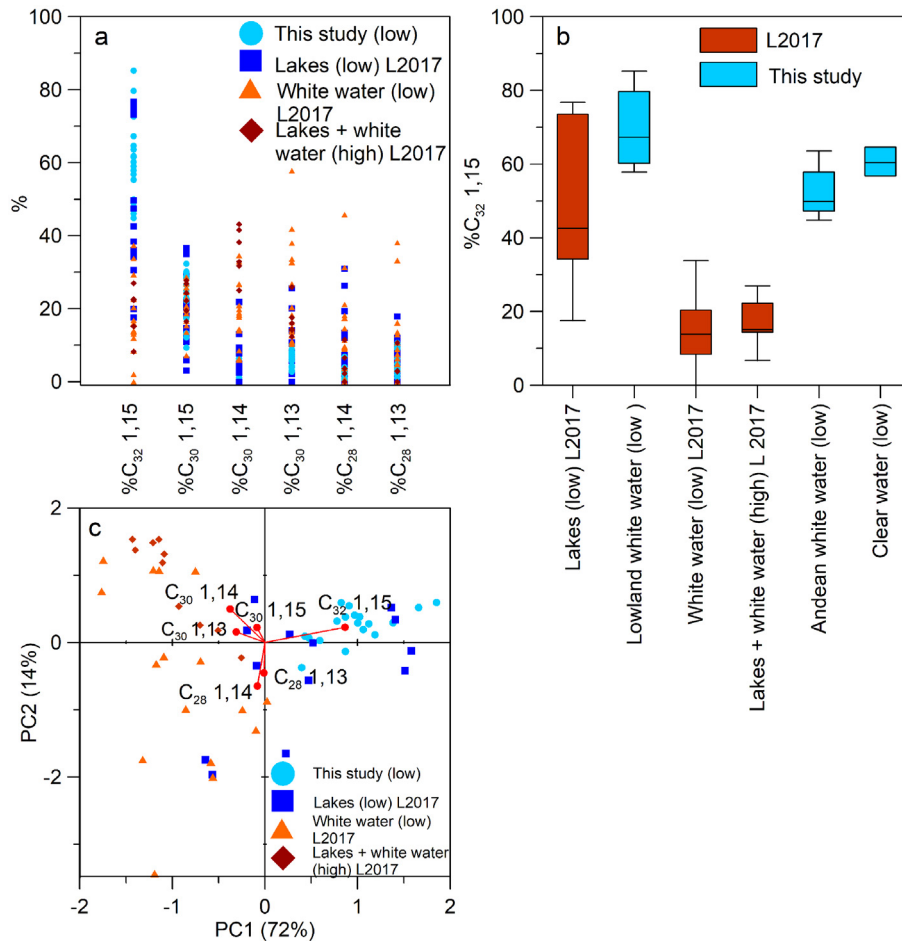
Fig. 3. Comparison of long-chain alkyl diol relative concentration data from this study to data from Lattaud et al. (2017b) indicated as "L2017", for samples of suspended sediments of the Amazon River system. (a) Comparison of the relative abundance of the C_{28-32} long-chain alkyl diols detected in the studied samples and by Lattaud et al. (2017b). (b) Boxplots comparing $\%C_{32}$ 1,15 for different Amazon River tributaries and seasonal water levels (i.e. high water and low water). (c) Principal component analysis (PCA) of the diol composition in suspended sediments from this study and Lattaud et al. (2017b). PC1 and PC2 are plotted on eigenvalue scale. Loadings for each LCD are indicated by red points. (For interpretation of the references to colour in this figure legend, the reader is referred to the web version of this article.)
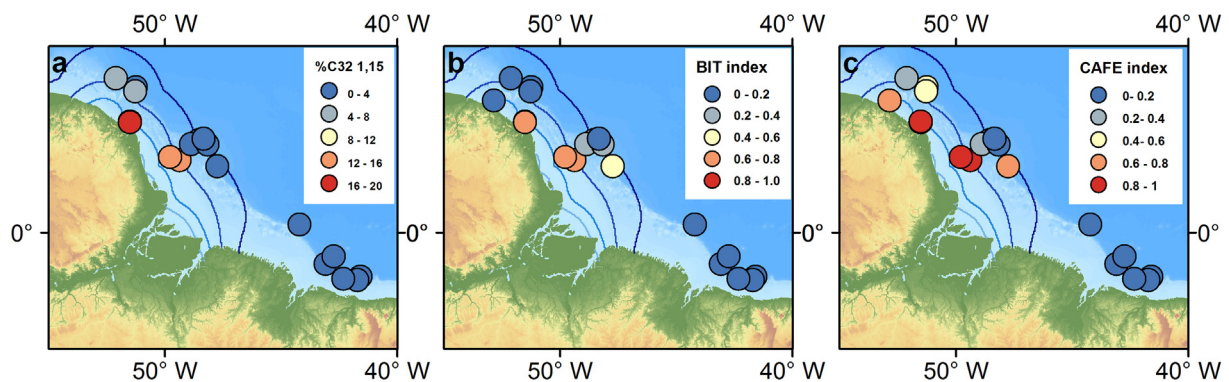

Fig. 4. Spatial distribution of the three studied proxies for terrestrial input to the northeast South American continental margin. (a) % C_{32} 1,15, (b) BIT index, (c) CAFE index (see Section 2.3 for the definition of the CAFE index). Blue contour lines in the Atlantic Ocean represent sea surface salinity indicating the north-westward flow of the Amazonian outflow (Sbrocco and Barber, 2013). (For interpretation of the references to colour in this figure legend, the reader is referred to the web version of this article.)
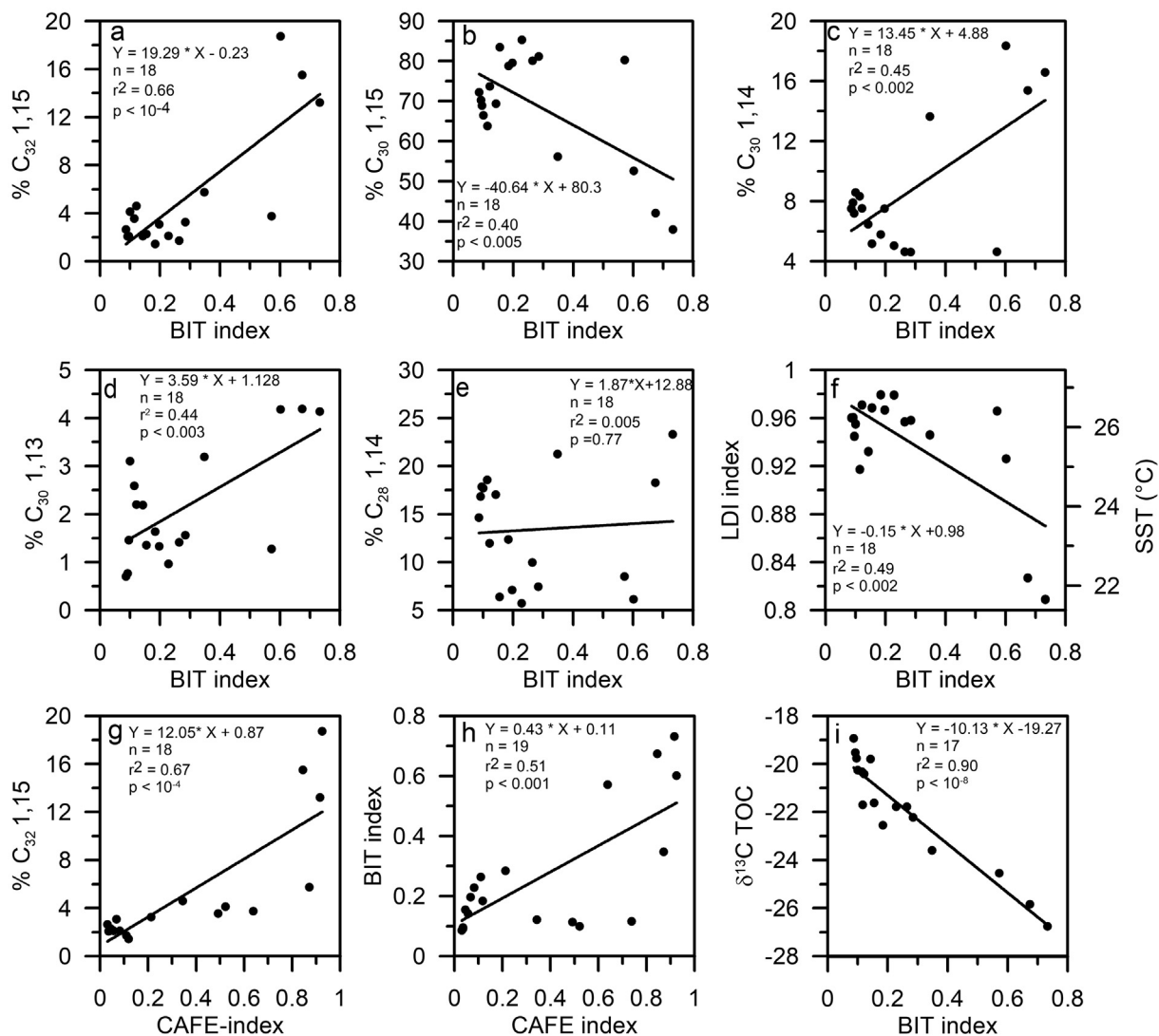
Fig. 5. Relation between the relative amount of long-chain alkyl diols and the BIT index in marine surface sediments from the north-eastern South American continental margin are shown in the upper two rows. (a) Correlation between BIT index and $\%C_{32}$ 1,15. (b) BIT index vs. $\%C_{30}$ 1,15. (c) BIT index vs. $\%C_{30}$ 1,14. (d) BIT index vs. $\%C_{30}$ 1,13. (e) BIT index vs. $\%C_{28}$ 1,14. (f) BIT index vs. long chain diol (LDI) index and LDI reconstructed sea surface temperature (SST). The relation between the CAFE index (see Section 2.3 for the definition of the CAFE index) and $\%C_{32}$ 1,15 (g) and the BIT index (h) as well as the correlation between the BIT index and bulk organic $\delta^{13}C$ (Sun et al., 2017) (i) are illustrated in the third row.

to the millennial trends observed in elemental ratios derived from XRF measurements, there are also long-term trends from lower BIT index values during MIS 3 to higher values during MIS 2 and a return to lower values during the deglaciation (Fig. 6d, Fig. 7). These trends are mirrored by the sediment accumulation rates recorded in the core (Fig. 6f), which have higher values during MIS 2, when the core was closer to the coast due to lower sea level.

Results of the LCD measurements in GeoB16224-1 show that the relative abundance of the C_{32} 1,15-LCD is lowest (i.e. 4%) during HS 1 and 3 with additional minima during other HS and Dansgaard Oeschger stadials (Fig. 6e). Highest values, up to 12%, are found during pronounced

DOI such as DOI 7 and 8. There is also a long-term trend towards lower values from MIS 3 to MIS 2. Overall, the trends observed in the C_{32} 1,15-LCD data contrast with those of the BIT and CAFE indices on both millennial (i.e. HS and DOI) and orbital (i.e. MIS 2 to MIS 3) time scales. $\%C_{28}$ 1,13 and 1,14 and the $\%C_{30}$ 1,13 and $\%C_{30}$ 1,14 values all follow a pattern similar to $\%C_{32}$ 1,15, with enhanced values during DOI and lower values during HS (Fig. 8c–f). Conversely, we find that $\%C_{30}$ 1,15 has higher values during HS and lower values during DOI (Fig. 8g). The difference between the relative C_{30} 1,15-LCD concentrations and the other studied LCDs is further supported by PCA analysis which shows opposite loadings in PC1
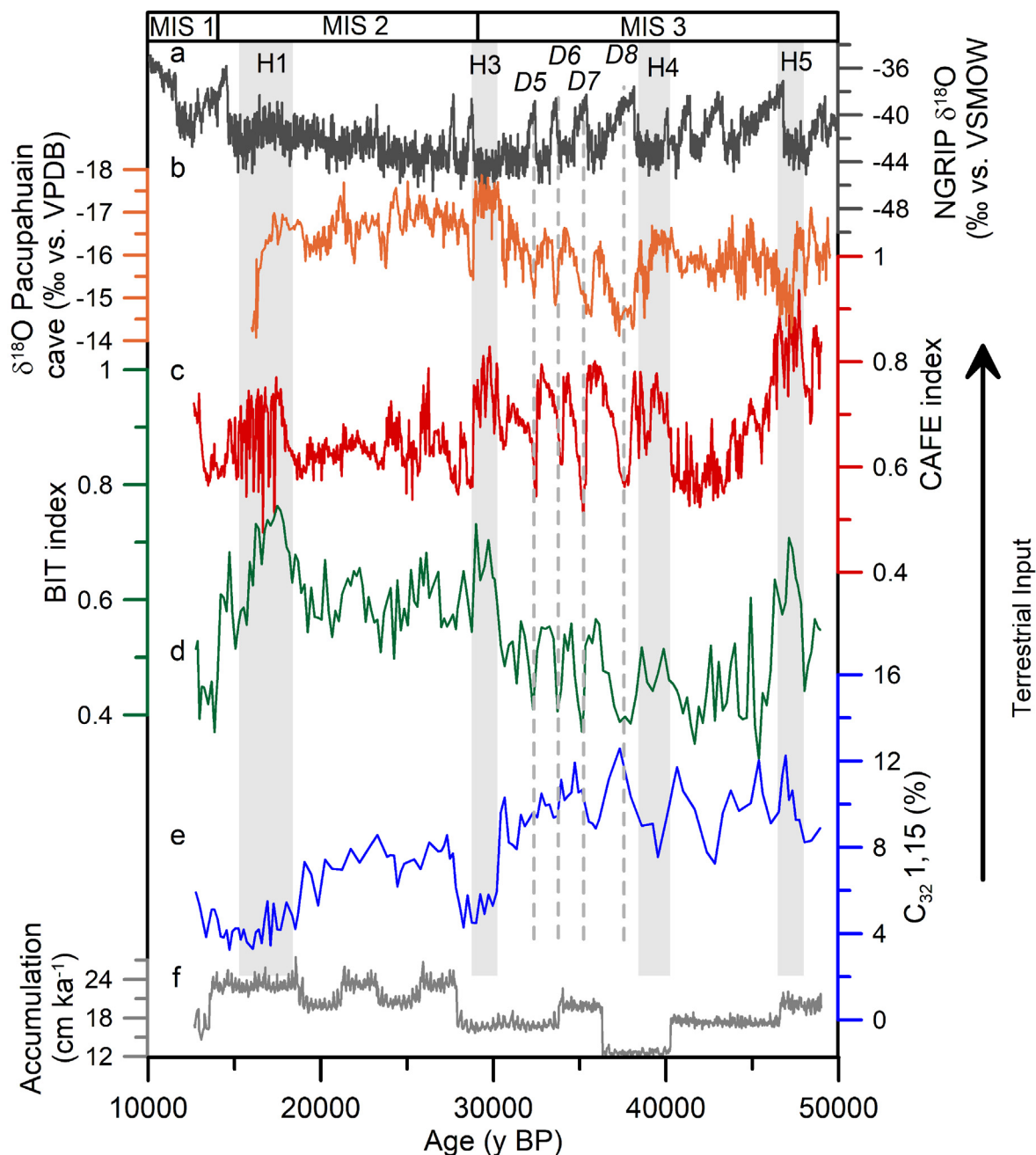
Fig. 6. Organic and inorganic proxies reflecting relative terrestrial input to GeoB16224-1 from the Amazon outflow plume during the late Pleistocene. (a) NGRIP ice core $\delta^{18}O$ record (NGRIP, 2004) on the GICC05 time-scale (Rasmussen, 2014). (b) $\delta^{18}O$ from the Pacupahuain Cave in the central Peruvian Andes (Kanner et al., 2012). (c) CAFE index. Data between 14 and 41 ka BP are derived from Zhang et al. (2017). (d) BIT index. Data between 14 and 22 ka BP is derived from Crivellari et al. (2018). (e) %C_{32} 1,15. (f) Sediment accumulation rate in core GeoB16224-1. The high frequency variability in the accumulation rate is an artifact of the Monte Carlo simulation used in the age model. The grey bars represent Heinrich stadials (H) 1, 3, 4 and 5. The dashed lines indicate the Dansgaard-Oeschger interstadials (D) 5–8 which are distinct in both the CAFE and BIT records. The boundaries of marine isotope stages (MIS) 1–3 are given on top.

(accounting for 83% of the variability) for the C_{30} 1,15-LCD compared to the rest of the studied LCDs (Fig. 9b). The LDI index also shows similar variations as the %C_{30} 1,15 with higher values during HS and lower values during DOI (Fig. 8h). Reconstructed LDI temperatures vary between 20 °C during DOI and 26 °C during HS (Fig. 8h).

4. DISCUSSION

4.1. Suspended sediments

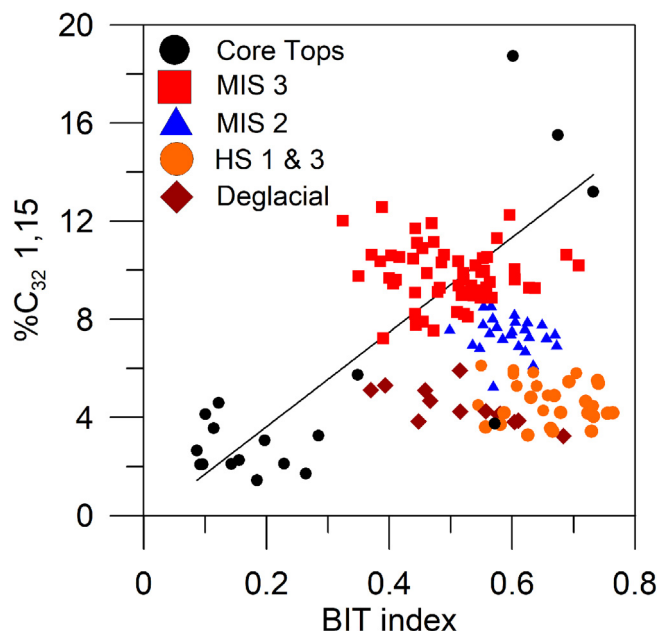Suspended sediments from the Amazon River and its main tributaries had overall high %C_{32} 1,15 values of

Fig. 7. Comparison of the BIT vs. %C$_{32}$ 1,15 relationship in marine surface sediments (as in Fig. 5a) to the down-core results of GeoB16224-1. Color coding differentiates between the core sections during MIS 3, MIS 2, HS 1 &3 and the deglacial following HS1.

>40% (Fig. 2a). Even though they had the lowest values in our sample set, the %C$_{32}$ 1,15 values for the Amazon main stem and the Madeira and Solimões rivers in our samples are higher (around 50%) than the ones reported for both wet and dry season sediment samples in a previous study (around 25%, Fig. 3b) (Lattaud et al., 2017b). The results from our 2015 dry season sediment samples more closely resemble the LCD distribution in sediments from flood-plain lakes of both black and white water types close to the Amazon main stem (Fig. 3b). Our data thus display a distinct seasonal variability in Amazonian LCD distributions not observed by Lattaud et al. (2017b). PCA of the suspended sediment LCDs also indicates that the LCD distributions in floodplain lakes along the Amazon main stem and in 2015 dry season sediment samples are similar (Fig. 3c). Samples collected during less pronounced dry and wet seasons from the Amazon main stem and white water tributaries have a distinctly different LCD distribution (Fig. 3c). Comparison of the %C$_{32}$ 1,15 from riverine suspended matter with marine sediments from the Amazon plume (around 20%) indicates that the Amazon main stem values of about 20% found for both the dry and wet season by Lattaud et al. (2017b) may be more typical than the higher values found in our dry season sample set (Figs. 3b and 5a).

The difference between samples from floodplain lakes and samples from riverine main channels (with the exception of the 2015 dry season) is likely caused by variable hydrological and sedimentary conditions of these water bodies. In floodplain lakes, the water bodies are stagnant and their sediment loads are deposited when the inflow to lakes from main channels is interrupted during the dry season. Both low turbidity and low flow rates favor higher primary productivity (Fisher and Parsley, 1979; Wissmar et al., 1981). Our data thus suggest that %C$_{32}$ 1,15 values are highest in environmental settings that favor maximal primary productivity and aquatic POC export in the Amazon River system (Wissmar et al., 1981; Hedges et al., 2000; Moreira-Turcq et al., 2013). The distinctive LCD distribution in the 2015 dry season can be similarly explained. During the 2015 dry season, a record drought occurred in the lowland Amazon Basin (Jiménez-Muñoz et al., 2016), contrasting with the more typical 2009 dry season, when the suspended sediment samples from Lattaud et al. (2017b) were taken. The extraordinarily dry conditions led to reduced flowrates and turbidity resulting in conditions more favourable to %C$_{32}$ 1,15 production. Moreover, our samples were taken close to the confluence of the tributaries to the main stem, where flow rates are low due to the back-water effect induced by the Amazon main stem and the formation of ria lakes in the case of the Tapajos, Xingu and Negro rivers (Archer, 2005). Floodplain lakes are also abundant at the confluence of the main tributaries and along the Amazon main stem. During pronounced dry seasons the inflow of water to floodplain lakes may stop, while the export of water and floodplain derived LCDs continues through the dry season (Rudorff et al., 2014). This may lead to the export of LCDs from stagnant water bodies and may explain the similarity of the 2015 dry season LCD distribution to that of floodplain lakes. Given that recent findings from the Rhine River point towards the presence of allochthonous LCDs in rivers (Lattaud et al., 2018), it is thus conceivable that the high %C$_{32}$ 1,15 values found in our dry season samples represent input from floodplain lakes.

Our samples from the 2015 dry season are derived from tributaries with a wide variation in water chemistry with pH values ranging from 4-5 in black water rivers to 6–7 in white
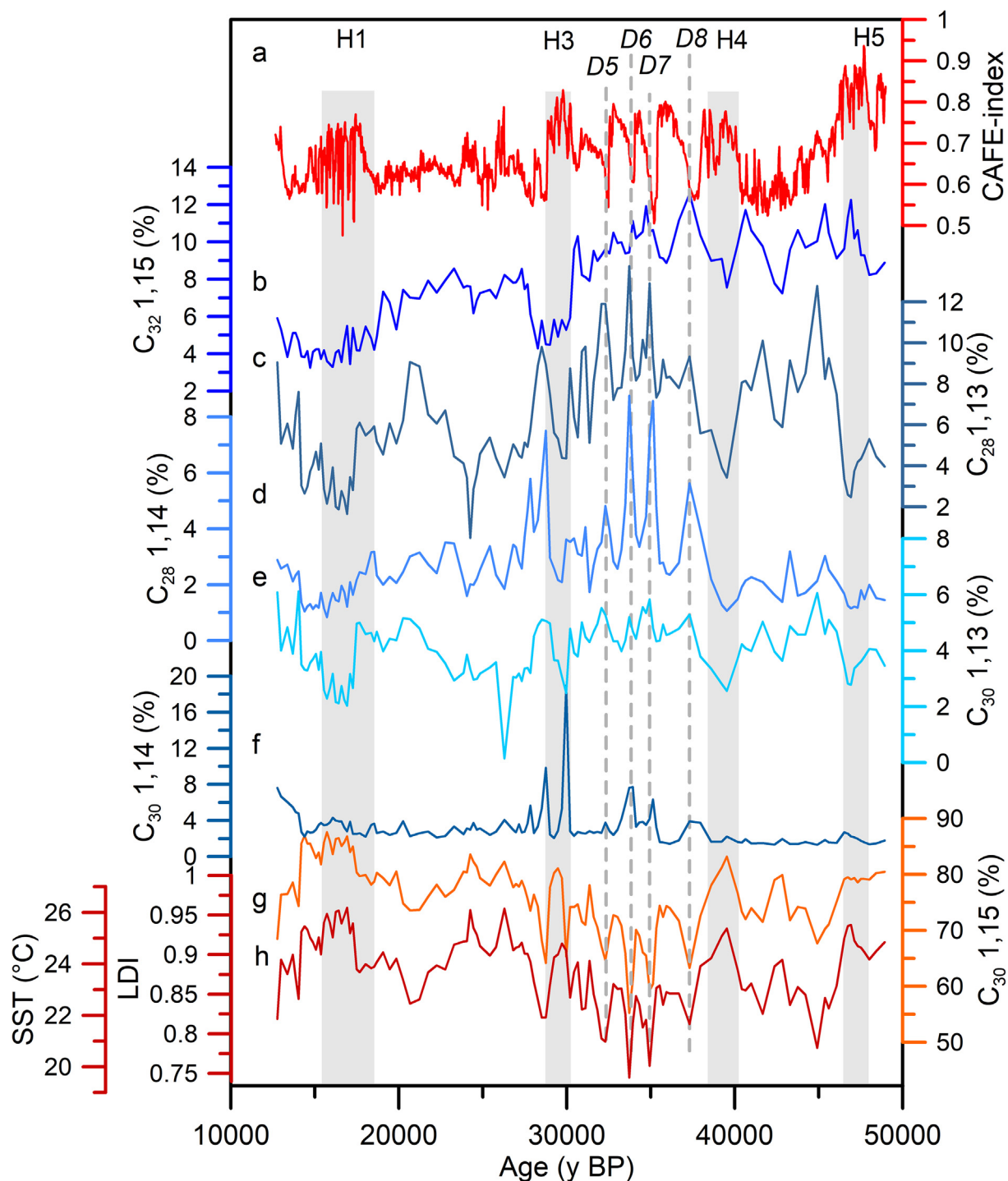
Fig. 8. Variations in the long chain alkyl diol composition in GeoB16224-1. (a) CAFE index as in Fig. 6. (b) %C$_{32}$ 1,15 as in Fig. 6. (c) %C$_{28}$ 1,13. (d) %C$_{28}$ 1,14. (e) %C$_{30}$ 1,13. (f) %C$_{30}$ 1,14. (g) %C$_{30}$ 1,15. (h) LDI index and reconstructed temperatures using the calibration by Rampen et al. (2012). Grey bars represent Heinrich stadials 1 and 3–5. The dashed lines indicate the Dansgaard-Oeschger interstadials 5–8 found to be distinct in the proxy records shown in Fig. 6.

water rivers (Sioli, 1984). Yet, their LCD distribution falls in the range of floodplain lakes and is distinct from dry and wet season channel samples from the Amazon River system found by Lattaud et al. (2017b). Hence, our data suggest that water chemistry is not the decisive factor controlling the LCD composition in the Amazon River system.

Rather, our findings point towards physical parameters such as water flow velocity and turbidity as key factors controlling riverine LCD composition.

Overall, our data set suggests two different modes of diol productivity (Fig. 3c). On the one hand, the C$_{32}$ 1,15-LCD is dominant in stagnant water bodies with low turbidity
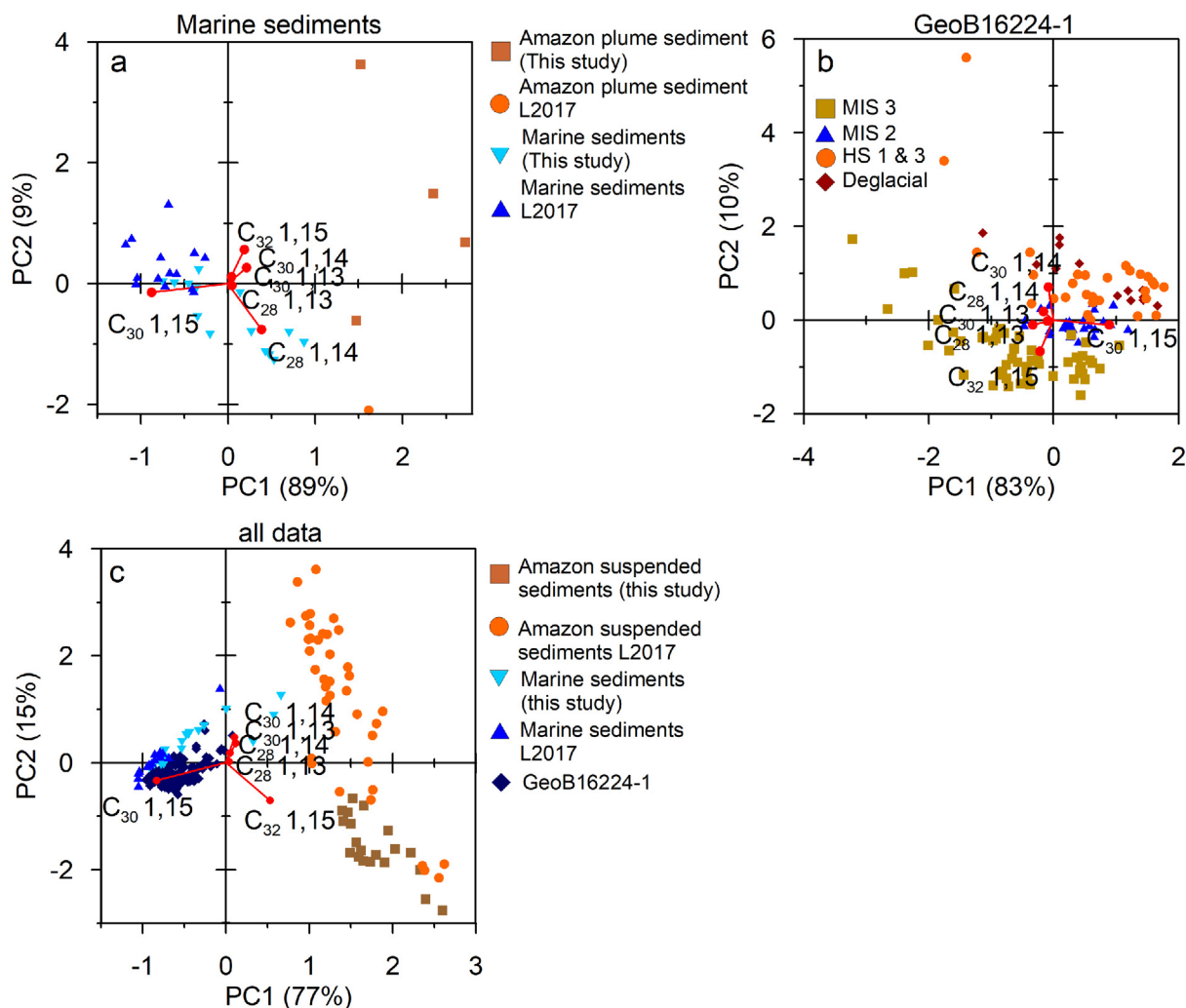
Fig. 9. Principal component analysis (PCA) of the diol distribution in suspended sediments, marine surface sediments and core GeoB16224-1. (a) PCA of the marine surface sediments. (b) PCA of GeoB16224-1.c) PCA of the entire data set including the suspended sediment and marine sediment data from Lattaud et al. (2017b) (L2017). PC1 and PC2 are plotted on eigenvalue scale. Loadings for each LCD are indicated by red points. (For interpretation of the references to colour in this figure legend, the reader is referred to the web version of this article.)

with minor contributions by the C_{30} 1,15-LCD, while the other LCDs are only present in low relative concentrations (Fig. 2b). On the other hand, %C_{32} 1,15 values are lower under more turbid riverine conditions, while the other LCDs (i.e. C_{28} 1,13 and 14, C_{30} 1,13 and 14) reach relative abundances up to 50% (Fig. 3a). Even though the identities of the organisms responsible for synthesizing LCDs remain elusive (Lattaud et al., 2018), this observation suggests that there are potentially different organisms responsible for LCD production in riverine main stems and floodplain lakes.

Deviation of dry season suspended sediment values from marine sediment values is also observed for the BIT index (Figs. 2c and 4b). Here, the values from the Amazon main stem are also lower than those in modern marine sediments. Similar observations were made by Kim et al. (2012), who found that dry season BIT index values from the Amazon River were lower than for the wet season, also indicating an enhanced proportional contribution of aquatic organic carbon during the dry season.

4.2. Marine surface sediments

4.2.1. Comparison of %C_{32} 1,15 to BIT and CAFE indices

The pattern seen in the marine surface sediments for all three analysed proxies (i.e. %C_{32} 1,15, BIT index and CAFE index) indicates that signals reflecting high terrestrial input are confined to the Amazon plume region (Fig. 4a–c), where modern sediments derived from the Amazon fluvial system are being deposited (Geyer et al., 1996). This finding is in agreement with previous studies on biomarker compositions in the studied region (i.e. the relative distribution of brGDGT concentrations and the isotopic composition of plant waxes and lignin phenols), where proxy values corresponding to an Amazonian signal were also limited to shelf areas (Zell et al., 2014; Häggi et al., 2016; Sun et al., 2017). As expected from their similar geographic distributions, the three proxies are positively correlated (Fig. 5a, g, h). They also correlate with the $\delta^{13}C$ composition of bulk organic matter (Sun et al., 2017) (Fig. 5i), which is also used as a proxy for the input of terrestrial organic matter. The

highest correlation coefficient ($r^2 = 0.90$) is found for the correlation between BIT index and $\delta^{13}C$ of bulk organic matter. This relationship can be explained by the fact that both $\delta^{13}C$ and BIT index reflect the input of terrestrial organic carbon, while the other proxies reflect the input of inorganic sediment and aquatic organic carbon. Since it is possible that the different carbon pools are associated with different grain size fractions of the riverine sediment, there might be slight variations in their coastal distribution. Moreover, there are likely variations in the productivity of the marine component of the proxies, since they rely on compounds produced by different marine organisms. Nevertheless, the correlation between $\%C_{32}$ 1,15 based on exclusively aquatically produced compounds and the BIT index based on brGDGTs, which have terrestrial and aquatic sources (Zell et al., 2014), is also significant ($r^2 = 0.66$; $p < 10^{-4}$). Thus, our results show that the modern distribution of proxies representing different riverine transported carbon and sediment pools is remarkably similar.

4.2.2. Comparison to other studies

The positive correlation between the $\%C_{32}$ 1,15 and the BIT index confirms earlier findings from coastal areas in Portugal (de Bar et al., 2016), the Gulf of Lion and the Berau delta (Lattaud et al., 2017b), as well as down-core studies off the Nile and Zambezi rivers, where the BIT index and the $\%C_{32}$ 1,15 also co-varied (Lattaud et al., 2017a). Our findings, however, contrast with those of an earlier study in the coastal area close to the Amazon River plume, where no such correlation was found (Lattaud et al., 2017b). This discrepancy can be explained by the fact that Lattaud et al. (2017b) studied only a few marine surface sediment samples with BIT index values >0.5, while most were much lower. If we only consider samples from our data set that have BIT index values <0.5, then significant correlation between the BIT index and the $\%C_{32}$ 1,15 is also absent.

The maximum riverine $\%C_{32}$ 1,15 contribution of 20% found for sediments influenced by the Amazon plume is lower than for sediments offshore of other major river systems. Studies for the Nile and Zambezi rivers showed river $\%C_{32}$ 1,15 endmembers >30% and similar values were reported for the Rhone River and the Portuguese margin (de Bar et al., 2016; Lattaud et al., 2017a,b). Moreover, $\%C_{32}$ 1,15 from the Arctic Kara Sea showed consistently high $\%C_{32}$ 1,15 values of 40–50% regardless of BIT index values. Conversely, values from the Berau delta in the Indonesian tropics were also around 20% for surface sediments with BIT indices close to 1 and thus comparable to our findings. While this comparison of different river delta areas seems to indicate lower $\%C_{32}$ 1,15 end member in the tropics, data from river suspended sediments do not show such a trend (Lattaud et al., 2018).

4.2.3. Fractional abundance of the C_{28} 1,13, C_{30} 1,13, C_{30} 1,14 and C_{30} 1,15-LCDs

Apart from the correlation between $\%C_{32}$ 1,15 and the BIT index, we also found that the fractional abundances of the C_{30} 1,13 and C_{30} 1,14-LCDs are positively correlated with the BIT index (Fig. 5c and d), while the fractional

abundance of the C_{30} 1,15-LCD are inversely correlated (Fig. 5b). Moreover, we find that the LDI temperature proxy is negatively correlated with BIT index values (Fig. 5f). The fractional abundances of C_{30} 1,13 and C_{30} 1,15 are highly temperature-dependent and used in the LDI proxy (Rampen et al., 2012). The C_{30} 1,15-LCD is typically the LCD-endmember found in tropical oceans, while the C_{30} 1,13 and C_{28} 1,13-LCDs are more abundant in higher latitudes. Given that mean annual water temperatures in the Amazon plume are slightly higher (28 °C) than in the surrounding tropical ocean (27 °C) (Locarnini et al., 2013), it is expected that the C_{30} 1,13 and C_{28} 1,13-LCDs should have similar or lower fractional abundances leading to higher LDI values in the vicinity of the Amazon plume. However, we find the opposite trend with higher C_{30} 1,13 abundances (Fig. 5d) and a lower LDI index leading to reconstructed temperatures as low as 24 °C (Fig. 5f) in the Amazon plume. Thus, our data suggest that the C_{30} 1,13-LCDs are at least partly of riverine origin or a result of primary productivity in the Amazon plume. This is supported by the high relative C_{30} 1,13 and C_{28} 1,13 abundances in suspended sediments of the Amazon River, where maximum values of 60% for C_{30} 1,13 and 40% for C_{28} 1,13 were detected (Fig. 3a) (Lattaud et al., 2017b). Moreover, PCA of the core top data also indicates opposite loading for the C_{30}, 1,15-LCD compared to the other analysed LCDs (Fig. 9a), in further support of the contention that LCDs other than C_{30}, 1,15 are either directly or indirectly of riverine origin in our marine sediments.

Our results suggest that LCD based temperature reconstructions under riverine influence can be systematically underestimated (Fig. 5f). Specifically, our data show that the LDI temperature proxy cannot be applied in situations where enhanced riverine LCD input with $\%C_{32}$ 1,15 values higher than 10% are observed. Outside the region impacted by the Amazon plume, where $\%C_{32}$ 1,15 values are minimal, the reconstructed temperatures of 27–29 °C are accurate within the calibration error of 2 °C (Rampen et al., 2012). A systematic underestimation in LDI derived temperatures close to a riverine estuary was also observed by de Bar et al. (2016) offshore Portugal and by Lattaud et al. (2017b) for the Rhone and Berau deltas. In the case of the LDI values from the Portuguese coast, there was doubt whether the low LDI values were indeed the result of riverine productivity or the result of altered marine productivity, perhaps due to indirect riverine influence (de Bar et al., 2016). Since the Amazon plume is a nutrient-rich environment with high primary productivity (Santos et al., 2008), the influence of variations in marine productivity cannot be ruled out. If productivity in the Amazon plume plays a role, it would still indicate a dominant riverine influence on the LDI values. In a similar way, the fractional abundances of the C_{30} 1,14-LCD also correlate with BIT index values (Fig. 5c). The C_{30} 1,14-LCD is usually not abundant in tropical oceans unaffected by upwelling (Rampen et al., 2012). C_{30} 1,14-LCDs of riverine origin might therefore also impact LCD-based upwelling proxies (Rampen et al., 2008). Alternatively, the C_{30} 1,14-LCDs found in the marine surface sediments underlying the Amazon plume could originate from riverine diatoms found in

the plume itself. Due to the high nutrient availability, the conditions could resemble upwelling environments favouring C_{30} 1,14-LCD productivity.

4.3. Down-core reconstructions

The close relation between the BIT and CAFE indices in marine gravity core GeoB16224-1 indicates that organic and inorganic terrestrial input into coastal waters co-varied in the period from 12.8 to 49 ka BP and showed elevated values during HS and decreased values during DOI (Fig. 6). This relationship contrasts with that for $\%C_{32}$ 1,15 which shows generally lower values during HS and higher ones during DOI, leading to a negative correlation between $\%C_{32}$ 1,15 and the BIT index ($r^2 = 0.29$, $p < 10^{-9}$, Figs. 6 and 7). The comparison between the long-term down-core variability and the modern correlation between $\%C_{32}$ 1,15 and BIT index reveals that most MIS 3 values fit well with the correlation found for marine surface sediments (Fig. 7). Samples from MIS 2, and especially from HS 1 and 3, deviate significantly from the modern regression line (Fig. 7). This contrasts with the positive correlation among the three proxies in marine modern surface sediments (Figs. 4 and 5a, g, h). It also contrasts with downcore reconstructions from the Nile and Zambezi Rivers, which have positive correlations between $\%C_{32}$ 1,15 and the BIT index (Lattaud et al., 2017a). While the C_{32} 1,15 is negatively correlated to the BIT and CAFE indices in the down-core record, the LCD distribution of the same down-core record is similar to that of the surface sediments. The C_{28} 1,13 and 1,14-LCDs, as well as C_{30} 1,13 and 1,14-LCDs, follow a pattern similar to C_{32} 1,15-LCD, while C_{30} 1,15-LCD follows the opposite pattern (Fig. 8). This is further indicated by PCA, which also shows opposite loadings for the C_{30} 1,15-LCD compared to the other analysed LCDs, similar to the modern situation (Fig. 9a and b). This finding again points towards a riverine source for the elevated C_{30} 1,13 and C_{30} 1,14 found in the marine surface sediments. Thus, our data indicate that LCD export of the Amazon River decreased (increased) during times of enhanced (lowered) terrestrial sediment input. This relationship holds for both millennial (i.e. Heinrich stadials) and orbital time-scales (i.e. sea level changes between MIS 2 and MIS 3).

The changes in both BIT index and LCD composition from MIS 3 to MIS 2 coincide with a 60–70 m drop in sea level (Lambeck et al., 2014). Sea level fall led to coastline regression and shifted the Amazon plume to a position closer to our core site, resulting in higher sedimentation rates (Fig. 6). Moreover, the drop in sea level from MIS 3 to MIS 2 also led to incision of the Amazon River channel and potentially enhanced erosion in the lowland basin, factors that also increased the sediment transport to our core site (Harris and Mix, 1999; Sant'Anna et al., 2017, Fig. 10). The increased lowland erosion also led to enhanced POC export due to soil erosion and the potential erosion of floodplain areas (Fig. 10). The incision of the Amazon channel led not only to a decrease in floodplain lakes and the backwater effect in lowland tributaries, but also to an increase in turbidity, both triggering unfavour-

able conditions for C_{32} 1,15-LCD production (Fig. 10). Furthermore, the precipitation amount was lower during MIS 2 than during MIS 3 (van der Hammen et al., 1992; Häggi et al., 2017), which further decreased the area and abundance of floodplain lakes and consequently C_{32} 1,15-LCD productivity. It is hard to asses whether the upstream propagation of erosion due to channel incision also led to the remobilization of sedimentary LCDs from the erosion of floodplains. Nevertheless, the observation that $\%C_{32}$ 1,15 values during the LGM were lower (Fig. 6e) suggests that remobilization of floodplain LCDs with typically high $\%C_{32}$ 1,15 values did not exert a dominant influence on the exported LCD composition.

The reduced $\%C_{32}$ 1,15 during Heinrich stadials coincided with an increase in sediment transport due to enhanced precipitation in the Andes (Kanner et al., 2012; Zhang et al., 2017) (Figs. 7b, c and 10b). The increase in sediment transport produced higher turbidity in the western tributaries draining the Andes and the Andean foreland resulting in less favourable conditions for C_{32} 1,15 production along the Amazon River. Both factors likely promoted a decrease of $\%C_{32}$ 1,15 in core GeoB16224-1 together with an increase in BIT index values due to higher soil material input (Fig. 10). Our results thus suggest that changes in climate, sediment load, and river morphology (e.g. channel incision and upstream propagation of erosion) that favoured terrestrial POC export impeded riverine POC export both on orbital and millennial timescales.

Alternatively, the shift in diol composition could also be caused by enhanced marine productivity during MIS 2 and Heinrich stadials. This is unlikely, however, given the fact that higher sediment input leads to light limitation (Smith and Russell, 1995) and reduced alkenone productivity within the plume (Häggi et al., 2015). Variations of marine productivity by autotrophic haptophyte algae, signalled by variations in alkenone accumulation rates, also indicate that productivity was lower during HS 1 and 4, and higher during DOI 7 (Zhang et al., 2017).

4.4. Synthesis and implications

4.4.1. Implications for LCD proxies

PCA of the diol distribution from the Amazon River and the western equatorial Atlantic exhibit different LCD distributions in the open marine and riverine environments. Sediments from the Amazon plume show an intermediate composition (Fig. 9c). PCA of the full data set indicates that the C_{30} 1,15-LCD is loaded opposite to the other LCDs for PC1 which accounts for 77% of the variability. This finding again indicates that C_{30} 1,15-LCD represents the marine end member while the other compounds are likely of riverine origin. Fig. 3a illustrates that all LCDs commonly found in open marine sediments (Rampen et al., 2012) are also found in relative concentrations of up to 40% in the Amazon River system. This includes C_{30} 1,15-LCD which is the dominant compound in tropical marine environments. Yet, riverine $\%C_{30}$ 1,15 is systematically below the 60–90% found in marine sediments, explaining the difference between riverine and marine LCD distributions (Fig. 9c). The variability of the riverine LCD
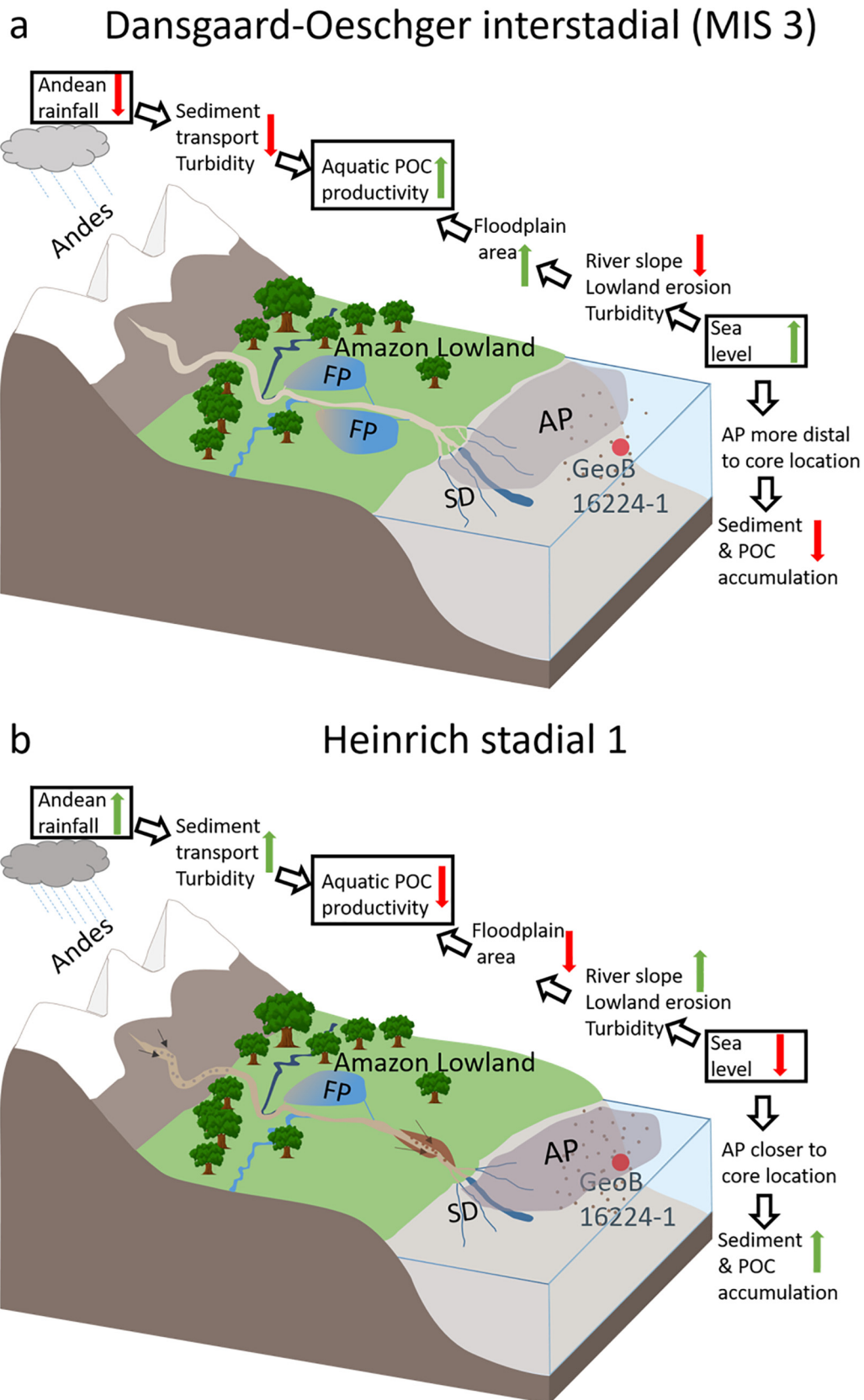
Fig. 10. Schematic overview of the influence of climate and sea level changes on sediment and aquatic and terrestrial particulate organic carbon (POC) export. (a) Situation during a generic Marine Isotope Stage (MIS) 3 Dansgaard-Oeschger interstadial (DOI). (b) Situation during Heinrich stadial (HS) 1. FP represents floodplains, SD the Amazon sub-aqueous delta, AP the Amazon plume and the dark arrows in the Andes and the lowland in (b) represent erosion.

follows mostly PC2 of the PCA analysis of the entire data set (Fig. 9c). For PC2, the C_{32} 1,15-LCD, which is dominant in stagnant water bodies, is again loaded in the opposite direction than the C_{28} 1,13, 1,14 and C_{30} 1,13, 1,14-LCDs, which have a higher relative abundance in riverine main stems. This further substantiates the conclusion that the C_{32} 1,15-LCD and the other studied LCDs are dominantly produced under different conditions.

The riverine input of the C_{28} 1,13, 1,14 and C_{30} 1,13, 1,14-LCDs, otherwise not abundant in tropical oceans, impacts the interpretation of LCD-based temperature and upwelling proxies in the vicinity of the Amazon River plume and leads to a general underestimation of reconstructed temperatures (Fig. 5f). The down-core pattern of the LDI temperature proxy yields reconstructed temperatures as low as 20 °C during DOI, when riverine LCD input is at maximum (Fig. 8h). Conversely, during HS, when the amount of riverine LCDs decreases, reconstructed temperatures are as high as 26 °C (Fig. 8h), despite the high terrestrial input indicated by high BIT index values during HS (Fig. 6d). Thus, we conclude that the lower LDI temperatures found in river plumes are likely an artefact caused by riverine derived LCDs.

The discrepancy between the $\%C_{32}$ 1,15 proxy and the BIT index found in our study also reveals the potential to reconstruct past changes in river characteristics based on the combined use of the two proxies. If down-core records of BIT index and $\%C_{32}$ 1,15 display similar trends, we would conclude that river characteristics remained stable (Fig. 7). An inverse relationship between the two proxies, on the other hand, would likely indicate major changes in river characteristics. A reduction of $\%C_{32}$ 1,15 during periods of enhanced BIT values would thus indicate a reduction in riverine POC productivity, while enhanced $\%C_{32}$ 1,15 during periods of lower BIT values would indicate an increase in aquatic POC.

4.4.2. Inorganic and organic matter transport in the Amazon River basin

Terrestrial inorganic and organic matter transport by the Amazon River system showed large variations during the last glacial that mostly coincided with HS and DOI events (Fig. 6) (Zhang et al., 2017; Crivellari et al., 2018). Rapid shifts in terrestrial inorganic and organic matter input recorded by the CAFE and BIT indices indicate a quick response of sediment transport to millennial climate variability in the Amazon Basin (Zhang et al., 2017). Remarkably, changes in the relative abundance of terrestrial sediment and POC accumulation in core GeoB16224-1 were recorded without delay by both proxies (Fig. 6c and d). Cosmogenic nuclide analyses in sediments from Amazonian rivers indicate extensive and prolonged sediment storage in the lowland Amazon Basin (Wittmann et al., 2011). Our data, however, suggest that the buffering effect of the lowland Amazon Basin does not prevent a fraction of the sedimentary pulses caused by increased Andean precipitation during HS to progress throughout the entire basin with a delay of less than a few decades. This fast progression of sedimentary signals during the late Pleistocene may have various explanations. First, it is conceivable that

sediment pulses were large enough to overcome the storage capacity of fluvial channels and floodplains in lowland Amazonia. Second, it is also possible that the storage capacity during the late Pleistocene was reduced compared to the present due to more incised fluvial valleys and the reduced floodplain area (Irion et al., 2009). Third, it is possible that the fine sediment fraction progresses more rapidly through the basin than the coarse-grained fraction, on which cosmic nuclides are measured (Wittmann et al., 2011). The rapid shifts in sediment transport during HS and DOI also led to a fast response in aquatic POC export to the western equatorial Atlantic (Fig. 8), which further demonstrates the high fidelity response of aquatic POC to shifts in climate and river morphology observed in our study.

5. CONCLUSIONS

We studied LCDs, elemental ratios and GDGT-based proxies in modern and late Pleistocene sediments from the Amazon River system and the adjacent western equatorial Atlantic. Analysing suspended sediments from the Amazon River and its tributaries, we show that $\%C_{32}$ 1,15 is highest in floodplain lakes along the Amazon River main stem and lowest in Andean white water tributaries. LCD distributions similar to the ones from floodplain lakes were also found in river suspended sediment samples from the extreme 2015 dry season. We suggest that the production of C_{32} 1,15 is highest in stagnant water bodies with low turbidity (e.g. floodplain lakes and lowland tributaries), while it is lowest under conditions of high turbidity and fast streamflow (e.g. Amazonian white water tributaries). Thus, we suggest that physical factors (e.g. flow velocity and turbidity) are more important than chemical variability (e.g. pH) found among the different Amazon tributaries in controlling the distribution of riverine LCD.

In marine surface sediment samples from the western equatorial Atlantic, the riverine $\%C_{32}$ 1,15 correlates well with the terrestrial organic (BIT index) and terrestrial inorganic (CAFE index) input. In a gravity core from the continental margin off French Guiana under the influence of Amazon outflow during the late Pleistocene, the BIT and CAFE indices showed similar trends with higher values during Heinrich stadials and lower values during Dansgaard-Oeschger interstadials. Moreover, BIT values were higher during MIS 2 than during MIS 3. This finding contrasts with $\%C_{32}$ 1,15, which had lower values during MIS 2 than during MIS 3 and lower values during Heinrich stadials than during Dansgaard-Oeschger interstadials. We interpret this anti-phased behaviour to arise from: (i) a reduction of floodplain lakes due to less humid conditions and sea level low stand during the LGM; and (ii) enhanced turbidity due to an increase in Andean sediment transport during Heinrich stadials. Both conditions led to a reduction in riverine LCD productivity, in general, and in C_{32} 1,15-LCD, in particular, and allowed for a more dominant role of marine-produced LCDs (i.e. C_{30} 1,15-LCD) at the core site. Thus, we conclude that terrestrial and aquatic carbon reservoirs in the Amazon Basin can show contrasting responses to past climate shifts.

Data availability statement

All data presented in this study is archived on www.pangaea.de.

APPENDIX A. SUPPLEMENTARY MATERIAL

Supplementary data to this article can be found online at https://doi.org/10.1016/j.gca.2019.07.018.

REFERENCES

Archer A. W. (2005) Review of Amazonian depositional systems. In *Fluvial Sedimentology VII* (eds. M. D. Blum, S. B. Marriott and S. Leclair). Blackwell Publishing Ltd, pp. 17–39.

Battin T. J., Kaplan L. A., Findlay S., Hopkinson C. S., Marti E., Packman A. I., Newbold J. D. and Sabater F. (2008) Biophysical controls on organic carbon fluxes in fluvial networks. *Nat. Geosci.* **1**, 95–100.

Bouchez J., Galy V., Hilton R. G., Gaillardet J., Moreira-Turcq P., Perez M. A., France- Lanord C. and Maurice L. (2014) Source, transport and fluxes of Amazon River particulate organic carbon: insights from river sediment depth-profiles. *Geochim. Cosmochim. Acta* **133**, 280–298.

Costa M. P. F., Novo E. M. L. M. and Telmer K. H. (2013) Spatial and temporal variability of light attenuation in large rivers of the Amazon. *Hydrobiologia* **702**, 171–190.

Crivellari S., Chiessi C. M., Kuhnert H., Häggi C., da Costa Portilho-Ramos R., Zeng J.-Y., Zhang Y., Schefuß E., Mollenhauer G., Hefter J., Alexandre F., Sampaio G. and Mulitza S. (2018) Increased Amazon freshwater discharge during late Heinrich Stadial 1. *Quat. Sci. Rev.* **181**, 144–155.

Damuth J. E. and Flood R. D. (1983) Morphology, sedimentation processes, and growth pattern of the Amazon Deep-Sea Fan. *Geo-Mar. Lett.* **3**, 109–117.

de Bar M. W., Dorhout D. J. C., Hopmans E. C., Rampen S. W., Sinninghe Damsté J. S. and Schouten S. (2016) Constraints on the application of long chain diol proxies in the Iberian Atlantic margin. *Org. Geochem.* **101**, 184–195.

de Leeuw J. W., Rijpstra W. I. C. and Schenck P. A. (1981) The occurrence and identification of C30, C31 and C32 alkan-1, 15-diols and alkan-15-one-1-ols in Unit I and Unit II Black Sea sediments. *Geochim. Cosmochim. Acta* **45**, 2281–2285.

Fisher T. R. and Parsley P. E. (1979) Amazon lakes: Water storage and nutrient stripping by algae1. *Limnol. Oceanogr.* **24**, 547–553.

Galy V., Peucker-Ehrenbrink B. and Eglinton T. (2015) Global carbon export from the terrestrial biosphere controlled by erosion. *Nature* **521**, 204–207.

Geyer W. R., Beardsley R. C., Lentz S. J., Candela J., Limeburner R., Johns W. E., Castro B. M. and Soares I. D. (1996) Physical oceanography of the Amazon shelf. *Cont. Shelf Res.* **16**, 575–616.

Gordon N. D., McMahon T. A., Finlayson B. L., Gippel C. J. and Nathan R. J. (2004) *Stream Hydrology An Introduction for Ecologists*, second ed. John Wiley & Sons, New York City.

Govin A., Holzwarth U., Heslop D., Keeling L. F., Zabel M., Mulitza S., Collins J. A. and Chiessi C. M. (2012) Distribution of major elements in Atlantic surface sediments (36°N-49°S): Imprint of terrigenous input and continental weathering. *Geochem. Geophys. Geosyst.* **13**, 23.

Häggi C., Chiessi C. M. and Schefuß E. (2015) Testing the D / H ratio of alkenones and palmitic acid as salinity proxies in the Amazon Plume. *Biogeosciences* **12**, 7239–7249.

Häggi C., Sawakuchi A. O., Chiessi C. M., Mulitza S., Mollenhauer G., Sawakuchi H. O., Baker P. A., Zabel M. and Schefuß E. (2016) Origin, transport and deposition of leaf-wax biomarkers in the Amazon Basin and the adjacent Atlantic. *Geochim. Cosmochim. Acta* **192**, 149–165.

Häggi C., Chiessi C. M., Merkel U., Mulitza S., Prange M., Schulz M. and Schefuß E. (2017) Response of the Amazon rainforest to late Pleistocene climate variability. *Earth Planet. Sci. Lett.* **479**, 50–59.

Hammer Ø., Harper D. A. T. and Ryan P. D. (2001) PAST: Paleontological statistics software package for education and data analysis. *Palaeontol. Electron.* **4**, 1–9.

Harris S. E. and Mix A. C. (1999) Pleistocene precipitation balance in the Amazon Basin recorded in deep sea sediments. *Quat. Res.* **51**, 14–26.

Hedges J. I., Ertel J. R., Quay P. D., Grootes P. M., Richey J. E., Devol A. H., Farwell G. W., Schmidt F. W. and Salati E. (1986) Organic Carbon-14 in the Amazon River system. *Science* **231**, 1129–1131.

Hedges J. I., Mayorga E., Tsamakis E., McClain M. E., Aufdenkampe A., Quay P., Richey J. E., Benner R., Opsahl S., Black B., Pimentel T., Quintanilla J. and Maurice L. (2000) Organic matter in Bolivian tributaries of the Amazon River: a comparison to the lower mainstream. *Limnol. Oceanogr.* **45**, 1449–1466.

Hopmans E. C., Schouten S., Pancost R. D., van der Meer M. T. J. and Sinninghe Damsté J. S. (2000) Analysis of intact tetraether lipids in archaeal cell material and sediments by high performance liquid chromatography/atmospheric pressure chemical ionization mass spectrometry. *Rapid Commun. Mass Spectrom.* **14**, 585–589.

Hopmans E. C., Weijers J. W. H., Schefuß E., Herfort L., Sinninghe Damsté J. S. and Schouten S. (2004) A novel proxy for terrestrial organic matter in sediments based on branched and isoprenoid tetraether lipids. *Earth Planet. Sci. Lett.* **224**, 107–116.

Hopmans E. C., Schouten S. and Sinninghe Damsté J. S. (2016) The effect of improved chromatography on GDGT-based palaeoproxies. *Org. Geochem.* **93**, 1–6.

Irion G., Müller J., Morais J. O., Keim G., de Mello J. N. and Junk W. J. (2009) The impact of Quaternary sea level changes on the evolution of the Amazonian lowland. *Hydrol. Process.* **23**, 3168–3172.

Kanner L. C., Burns S. J., Cheng H. and Edwards R. L. (2012) High-latitude forcing of the South American summer monsoon during the last glacial. *Science* **335**, 570–573.

Jiménez-Muñoz J. C., Mattar C., Barichivich J., Santamaría-Artigas A., Takahashi K., Malhi Y., Sobrino J. A. and Schrier G. v. d. (2016) Record-breaking warming and extreme drought in the Amazon rainforest during the course of El Niño 2015–2016. *Scientific Reports* **6**, 33130.

Kim J. H., Zell C., Moreira-Turcq P., Perez M. A. P., Abril G., Mortillaro J. M., Weijers J. W. H., Meziane T. and Damste J. S. S. (2012) Tracing soil organic carbon in the lower Amazon River and its tributaries using GDGT distributions and bulk organic matter properties. *Geochim. Cosmochim. Acta* **90**, 163–180.

Konhauser K. O., Fyfe W. S. and Kronberg B. I. (1994) Multi-element chemistry of some Amazonian waters and soils. *Chem. Geol.* **111**, 155–175.

Lambeck K., Rouby H., Purcell A., Sun Y. Y. and Sambridge M. (2014) Sea level and global ice volumes from the Last Glacial Maximum to the Holocene. *Proc. Natl. Acad. Sci. USA* **111**, 15296–15303.

Latrubesse E. M., Arima E. Y., Dunne T., Park E., Baker V. R., d'Horta F. M., Wight C., Wittmann F., Zuanon J., Baker P. A., Ribas C. C., Norgaard R. B., Filizola N., Ansar A., Flyvbjerg B. and Stevaux J. C. (2017) Damming the rivers of the Amazon basin. *Nature* **546**, 363–369.

Lattaud J., Dorhout D., Schulz H., Castañeda I. S., Schefuß E., Sinninghe Damsté J. S. and Schouten S. (2017a) The C32 alkane-1,15-diol as a proxy of late Quaternary riverine input in coastal margins. *Clim. Past* **13**, 1049–1061.

Lattaud J., Kim J.-H., De Jonge C., Zell C., Sinninghe Damsté J. S. and Schouten S. (2017b) The C32 alkane-1,15-diol as a tracer for riverine input in coastal seas. *Geochim. Cosmochim. Acta* **202**, 146–158.

Lattaud J., Kirkels F., Peterse F., Freymond C. V., Eglinton T. I., Hefter J., Mollenhauer G., Balzano S., Villanueva L., van der Meer M. T. J., Hopmans E. C., Sinninghe Damsté J. S. and Schouten S. (2018) Long-chain diols in rivers: distribution and potential biological sources. *Biogeosciences* **15**, 4147–4161.

Locarnini R. A., Mishonov A. V., Antonov J. I., Boyer T. P., Garcia H. E., Baranova O. K., Zweng M. M., Paver C. R., Reagan J. R., Johnson D. R., Hamilton M. and Seidov D. (2013) World Ocean Atlas 2013, Volume 1: Temperature. In NOAA Atlas NESDIS 73 (eds. S. Levitus and A. Mishonov, Technical Ed.). pp. 40.

Loncke L., Droz L., Gaullier V., Basile C., Patriat M. and Roest W. (2009) Slope instabilities from echo-character mapping along the French Guiana transform margin and Demerara abyssal plain. *Mar. Petrol. Geol.* **26**, 711–723.

McClain M. E. and Naiman R. J. (2008) Andean influences on the biogeochemistry and ecology of the Amazon River. *Bioscience* **58**, 325–338.

Meade R. H., Dunne T., Richey J. E., De M., Santos U. and Salati E. (1985) Storage and remobilization of suspended sediment in the Lower Amazon River of Brazil. *Science* **228**, 488–490.

Moreira-Turcq P., Bonnet M.-P., Amorim M., Bernardes M., Lagane C., Maurice L., Perez M. and Seyler P. (2013) Seasonal variability in concentration, composition, age, and fluxes of particulate organic carbon exchanged between the floodplain and Amazon River. *Glob. Biogeochem. Cycle* **27**, 119–130.

Mulitza S., Chiessi C. M., Cruz A. P. S., Frederichs T., Gomes J. G., Gurgel M. H., Haberkern J., Huang E., Jovane L., Kuhnert H., Pittauerová D., Reiners S.-J., Roud S. C., Schefuß E., Schewe F., Schwenk T. A., Sicoli Seoane J. C., Sousa S. H. M., Wagner D. J. and Wiers S. (2013) Response of Amazon sedimentation to deforestation, land use and climate variability – Cruise No. MSM20/3 - February 19 - March 11, 2012 - Recife (Brazil) - Bridgetown (Barbados). Berichte, Fachbereich Geowissenschaften, Universität Bremen, Bremen, Germany, pp. 1–86.

Muller-Karger F. E., McClain C. R. and Richardson P. L. (1988) The dispersal of the Amazon's water. *Nature* **333**, 56–59.

Nace T. E., Baker P. A., Dwyer G. S., Silva C. G., Rigsby C. A., Burns S. J., Giosan L., Otto-Bliesner B., Liu Z. and Zhu J. (2014) The role of North Brazil Current transport in the paleoclimate of the Brazilian Nordeste margin and paleoceanography of the western tropical Atlantic during the late Quaternary. *Palaeogeogr. Palaeoclimatol. Palaeoecol.* **415**, 3–13.

Rampen S. W., Schouten S., Koning E., Brummer G.-J. A. and Sinninghe Damsté J. S. (2008) A 90 kyr upwelling record from the northwestern Indian Ocean using a novel long-chain diol index. *Earth Planet. Sci. Lett.* **276**, 207–213.

Rampen S. W., Willmott V., Kim J.-H., Uliana E., Mollenhauer G., Schefuß E., Sinninghe Damsté J. S. and Schouten S. (2012) Long chain 1,13- and 1,15-diols as a potential proxy for palaeotemperature reconstruction. *Geochim. Cosmochim. Acta* **84**, 204–216.

Rampen S. W., Datema M., Rodrigo-Gámiz M., Schouten S., Reichart G.-J. and Sinninghe Damsté J. S. (2014) Sources and proxy potential of long chain alkyl diols in lacustrine environments. *Geochim. Cosmochim. Acta* **144**, 59–71.

Richey J. E., Hedges J. I., Devol A. H., Quay P. D., Victoria R., Martinelli L. and Forsberg B. R. (1990) Biogeochemistry of carbon in the Amazon River. *Limnol. Oceanogr.* **35**, 352–371.

Rudorff C. M., Melack J. M. and Bates P. D. (2014) Flooding dynamics on the lower Amazon floodplain: 2. Seasonal and interannual hydrological variability. *Water Resour. Res.* **50**, 635–649.

Salimon C., dos Santos Sousa E., Alin S. R., Krusche A. V. and Ballester M. V. (2013) Seasonal variation in dissolved carbon concentrations and fluxes in the upper Purus River, southwestern Amazon. *Biogeochemistry* **114**, 245–254.

Sant'Anna L. G., do Amaral Soares E. A., Riccomini C., Tatumi S. H. and Yee M. (2017) Age of depositional and weathering events in Central Amazonia. *Quat. Sci. Rev.* **170**, 82–97.

Santos M. L. S., Muniz K., Barros-Neto B. and Araujo M. (2008) Nutrient and phytoplankton biomass in the Amazon River shelf waters. *An. Acad. Bras. Cienc.* **80**, 703–717.

Sbrocco E. J. and Barber P. H. (2013) MARSPEC: ocean climate layers for marine spatial ecology. *Ecology* **94**, 979–979.

Shimokawara M., Nishimura M., Matsuda T., Akiyama N. and Kawai T. (2010) Bound forms, compositional features, major sources and diagenesis of long chain, alkyl mid-chain diols in Lake Baikal sediments over the past 28,000 years. *Org. Geochem.* **41**, 753–766.

Sinninghe Damsté J. S., Rampen S., Rijpstra W. I. C., Abbas B., Muyzer G. and Schouten S. (2003) A diatomaceous origin for long-chain diols and mid-chain hydroxy methyl alkanoates widely occurring in quaternary marine sediments: indicators for high-nutrient conditions. *Geochim. Cosmochim. Acta* **67**, 1339–1348.

Sioli H. (1984) The Amazon and its main affluents: Hydrography, morphology of the river courses, and river types. In *The Amazon: Limnology and Landscape Ecology of a Mighty Tropical River and its Basin* (ed. H. Sioli). Springer Netherlands, Dordrecht, pp. 127–165.

Smith W. O. and Russell G. J. (1995) Phytoplankton biomass and nutrient distributions in the Amazon river plume: environmental correlates. *Geo-Mar. Lett.* **15**, 195–198.

Sun S., Schefuß E., Mulitza S., Chiessi C. M., Sawakuchi A. O., Zabel M., Baker P. A., Hefter J. and Mollenhauer G. (2017) Origin and processing of terrestrial organic carbon in the Amazon system: lignin phenols in river, shelf, and fan sediments. *Biogeosciences* **14**, 2495–2512.

van der Hammen T., Duivenvoorden J. F., Lips J. M., Urrego L. E. and Espejo N. (1992) Late quaternary of the middle Caquetá River area (Colombian Amazonia). *J. Quatern. Sci.* **7**, 45–55.

Versteegh G. J. M., Bosch H. J. and De Leeuw J. W. (1997) Potential palaeoenvironmental information of C24 to C36 mid-chain diols, keto-ols and mid-chain hydroxy fatty acids; a critical review. *Org. Geochem.* **27**, 1–13.

Versteegh G. J. M., Jansen J. H. F., Schneider R. R. and De Leeuw J. W. (2000) Mid-chain diols and keto-ols in se atlantic sediments: a new tool for tracing past sea surface water masses? *Geochim. Cosmochim. Acta* **64**, 1879–1892.

Villanueva L., Besseling M., Rodrigo-Gámiz M., Rampen S. W., Verschuren D. and Sinninghe Damsté J. S. (2014) Potential biological sources of long chain alkyl diols in a lacustrine system. *Org. Geochem.* **68**, 27–30.

Volkman J. K., Barrett S. M. and Blackburn S. I. (1999) Eustigmatophyte microalgae are potential sources of C29 sterols, C22–C28 n-alcohols and C28–C32 n-alkyl diols in freshwater environments. *Org. Geochem.* **30**, 307–318.

Wissmar R. C., Richey J. E., Stallard R. F. and Edmond J. M. (1981) Plankton metabolism and carbon processes in the Amazon River, its tributaries, and floodplain waters, Peru-Brazil, May-June 1977. *Ecology* **62**, 1622–1633.

Wittmann H., von Blanckenburg F., Maurice L., Guyot J. L., Filizola N. and Kubik P. W. (2011) Sediment production and delivery in the Amazon River basin quantified by in situ-produced cosmogenic nuclides and recent river loads. *Geol. Soc. Am. Bull.* **123**, 934–950.

Zell C., Kim J. H., Moreira-Turcq P., Abril G., Hopmans E. C., Bonnet M. P., Sobrinho R. L. and Sinnignhe Damsté J. S. (2013) Disentangling the origins of branched tetraether lipids and crenarchaeol in the lower Amazon River: Implications for GDGT-based proxies. *Limnol. Oceanogr.* **58**, 343–353.

Zell C., Kim J.-H., Hollander D., Lorenzoni L., Baker P., Silva C. G., Nittrouer C. and Sinninghe Damsté J. S. (2014) Sources and distributions of branched and isoprenoid tetraether lipids on the Amazon shelf and fan: Implications for the use of GDGT-based proxies in marine sediments. *Geochim. Cosmochim. Acta* **139**, 293–312.

Zhang Z., Metzger P. and Sachs J. P. (2011) Co-occurrence of long chain diols, keto-ols, hydroxy acids and keto acids in recent sediments of Lake El Junco, Galápagos Islands. *Org. Geochem.* **42**, 823–837.

Zhang Y., Chiessi C. M., Mulitza S., Zabel M., Trindade R. I. F., Hollanda M., Dantas E. L., Govin A., Tiedemann R. and Wefer G. (2015) Origin of increased terrigenous supply to the NE South American continental margin during Heinrich Stadial 1 and the Younger Dryas. *Earth Planet. Sci. Lett.* **432**, 493–500.

Zhang Y., Chiessi C. M., Mulitza S., Sawakuchi A. O., Häggi C., Zabel M., Portilho-Ramos R. C., Schefuß E., Crivellari S. and Wefer G. (2017) Different precipitation patterns across tropical South America during Heinrich and Dansgaard-Oeschger stadials. *Quat. Sci. Rev.* **177**, 1–9.

Associate editor: Josef P. Werne